W. J. Minkowycz and E. M. Sparrow (Eds), Advances in Numerical Heat Transfer,
vol. 2, Chap. 6, pp. 189-226, Taylor & Francis, New York, 2000.

CHAPTER
SIX

MOLECULAR DYNAMICS METHOD FOR MICROSCALE HEAT TRANSFER

Shigeo Maruyama

1 INTRODUCTION

Molecular level understandings and treatments have been recognized to be more and more important in heat and mass transfer research. A new field, "Molecular Thermophysical Engineering," has a variety of applications in further development of macroscopic heat transfer theory and in handling the extreme heat transfer situations related to advanced technologies.

For example, studies of basic mechanisms of heat transfer such as in phase change heat transfer demand the microscopic understanding of liquid-solid contact phenomena. The nucleation theory of liquid droplet in vapor or of vapor bubble in liquid sometimes needs to take account of nuclei in size of molecular clusters. The efficient heat transfer in three-phase interface (evaporation and condensation of liquid on the solid surface) becomes the singular problem in the macroscopic treatment. Some modeling of the heat transfer based on the correct understandings of molecular level phenomena seems to be necessary. The effect of the surfactant on the heat and mass transfer through liquid-vapor interface is also an example of the direct effect of molecular scale phenomena on the macroscopic problem. The surface treatment of the solid surface has a similar effect.

Even though there has been much effort of extending our macroscopic analysis to extremely microscopic conditions in space (micrometer scale and nanometer scale system), time (microsecond, nanosecond and picosecond technology), and rate (extremely high heat flux), there is a certain limitation in the extrapolations. Here, the development of the molecular dynamics (MD) computer simulation technique has shown the possibility of taking care of such microscale phenomena from the other direction. The MD methods have long been used and are well developed as a tool in statistical mechanics and chemistry. However, it is a new challenge to extend the method to the spatial and temporal scale of

macroscopic heat transfer phenomena. On the other hand, by developments of high energy-flux devices such as laser beam and electron beam, more physically reasonable treatment of heat transfer is being required. The thin film technology developed in the semiconductor industry demands the prediction of heat transfer characteristics of nanometer scale materials.

In this chapter, one of the promising numerical techniques, the classical molecular dynamics method, is first overviewed with a special emphasis on applications to heat transfer problems in section 2 in order to give the minimum knowledge of the method to a reader not familiar with it. The van der Waals interaction potential for rare gas, effective pair potential for water and many-body potential for silicon and carbon are discussed in detail. Then, the molecular scale representation of the liquid-vapor interface is discussed in section 3. The surface tension, Young-Laplace equation, and condensation coefficient are discussed from the viewpoint of molecular scale phenomena. Section 4 deals with the solid-liquid-vapor interactions. MD simulations of liquid droplet in contact with solid surface and a vapor bubble on solid surface are introduced. The validity of Young's equation of contact angle is also discussed. Then, demonstrations of real heat transfer phenomena are discussed in section 4. Since heat transfer is intrinsically a non-equilibrium phenomenon, the non-equilibrium MD simulations for constant heat flux system and the homogeneous nucleation of liquid droplet in supersaturated vapor and nucleation of vapor bubble in liquid are discussed. Then, the heterogeneous nucleation of vapor bubble on the surface is also discussed. Some interesting non-equilibrium MD simulations dealing with the formation of molecular structures are introduced in section 5.4. Finally, in section 6, future developments of molecular scale heat transfer are discussed.

2 MOLECULAR DYNAMICS METHOD

Knowledge of statistical mechanical gas dynamics has been helpful to understand the relationship between molecular motion and macroscopic gas dynamics phenomena [1]. Recently, a direct simulation method using the Monte Carlo technique (DSMC) developed by Bird [2] has been widely used for the practical simulations of rarefied gas dynamics. In the other extreme, statistical mechanical treatment of solid-state matters has been well developed as solid state physics [e.g. 3]. For example, the direct simulation of the Boltzmann equation of phonon is being developed and applied to the heat conduction analysis of thin film [4] for example. However, when we need to take care of liquid or inter-phase phenomenon, which is inevitable for phase-change heat transfer, the statistical mechanics approach is not as much developed as for the gas-dynamics statistics and the solid-state statistics. The most powerful tool for the investigation of the microscopic phenomena in heat transfer is the MD method [e.g. 5]. In principal, the MD method can be applied to all phases of gas, liquid and solid and to interfaces of these three phases.

2.1 Equation of Motion and Potential Function

In the MD method, the classical equations of motion (Newton's equations) are solved for atoms and molecules as

$$m_i \frac{d^2 \boldsymbol{r}_i}{dt^2} = \boldsymbol{F}_i = -\frac{\partial \boldsymbol{\Phi}}{\partial \boldsymbol{r}_i}, \tag{1}$$

where m_i, $\boldsymbol{r}_i$, $\boldsymbol{F}_i$ are mass, position vector, force vector of molecule i, respectively, and $\boldsymbol{\Phi}$ is the potential of the system. This classical form of equation of motion is known to be a good approximation of the Schrödinger equation when the mass of atom is not too small and the system temperature is not too low. Equation (1) itself should be questioned when applied to light molecules such as hydrogen and helium and/or at very low temperature. Once the potential of a system is obtained, it is straightforward to numerically solve Eq. (1). In principal, any of gas, liquid, solid states, and inter-phase phenomena can be solved without the knowledge of "thermo-physical properties" such as thermal conductivity, viscosity, latent heat, saturation temperature and surface tension.

The potential of a system $\boldsymbol{\Phi}(\boldsymbol{r}_1, \boldsymbol{r}_2, ...\boldsymbol{r}_N)$ can often be reasonably assumed to be the sum of the effective pair potential $\phi(r_{ij})$ as

$$\boldsymbol{\Phi} = \sum_i \sum_{j>i} \phi(r_{ij}), \tag{2}$$

where r_{ij} is the distance between molecules i and j. It should be noted that the assumption of Eq. (2) is often employed for simplicity even though the validity is questionable. The covalent system such as carbon and silicon cannot accept the pair-potential approximation.

2.2 Examples of Potential Forms

In order to simulate practical molecules, the determination of the suitable potential function is very important. Here, the well-known Lennard-Jones potential for inert gas and for a statistical mechanical model system is introduced; also introduced are potential forms for water and many-body potential for silicon and carbon. The interaction potential forms between metal atoms are intentionally excluded because the luck of the effective technique of handling free electron for heat conduction prevents from the reasonable treatment of heat conduction through solid metal.

2.2.1 Lennard-Jones potential. An example of the pair potential is the well-known Lennard-Jones (12-6) potential function expressed as

$$\phi(r) = 4\varepsilon \left[\left(\frac{\sigma}{r} \right)^{12} - \left(\frac{\sigma}{r} \right)^{6} \right], \tag{3}$$

Table 1 Parameters for Lennard-Jones potential for inert molecules.

	σ [nm]	ε [J]	ε/k_B [K]
Ne	0.274	0.50×10^{-21}	36.2
Ar	0.340	1.67×10^{-21}	121
Kr	0.365	2.25×10^{-21}	163
Xe	0.398	3.20×10^{-21}	232

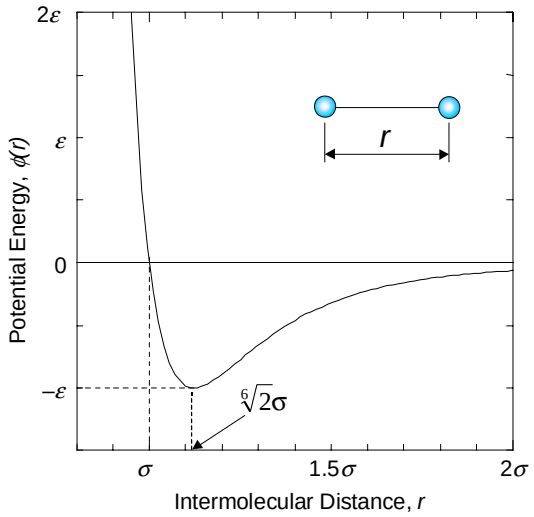

Figure 1 Lennard-Jones (12-6) potential.

where ε and σ are energy and length scales, respectively, and r is the intermolecular distance as shown in Fig. 1. The intermolecular potential of inert monatomic molecules such as Ne, Ar, Kr and Xe is known to be reasonably expressed by this function. Typical values of σ and ε for each molecule are listed in Table 1. Moreover, many computational and statistical mechanical studies have been performed with this potential as the model pair potential. Here, the equation of motion can be non-dimensionalized by choosing σ, ε and m as length, energy and mass scale, respectively. The reduced formulas for typical physical properties are listed in Table 2. When a simulation system consists of only Lennard-Jones molecules, the non-dimensional analysis has an advantage in order not to repeat practically the same simulation. Then, molecules are called Lennard-Jones molecules, and argon parameters σ = 0.34 nm, ε = 1.67×10^{-21} J, and τ = 2.2×10^{-12} s are used to describe dimensional values in order to illustrate the physical meaning. The phase-diagram of Lennard-Jones system [6] is useful for a design of a simulation. The critical and triplet temperatures are T_c^* = 1.35 and T_t^* = 0.68, or T_c = 163 K and T_t = 82 K with argon property [7].

For the efficient calculation of potential, which is the most CPU demanding, Lennard-Jones function in Eq. (3) is often cutoff at the intermolecular distance r_C = 2.5 σ to 5.5 σ. However, for pressure or stress calculations, the contribution to potential from far-away molecules can result in a considerable error as demonstrated for surface tension [8]. In order to reduce this discrepancy,

Table 2 Reduced properties for Lennard-Jones system.

Property		Reduced Form
Length	$r^* =$	r/σ
Time	$t^* =$	$t/\tau = t(\varepsilon/m\sigma^2)^{1/2}$
Temperature	$T^* =$	$k_B T/\varepsilon$
Force	$f^* =$	$f\sigma/\varepsilon$
Energy	$\phi^* =$	ϕ/ε
Pressure	$P^* =$	$P\sigma^3/\varepsilon$
Number density	$N^* =$	$N\sigma^3$
Density	$\rho^* =$	$\sigma^3\rho/m$
Surface tension	$\gamma^* =$	$\gamma\sigma^2/\varepsilon$

several forms of smooth connection of cutoff have been proposed such as in Eq. (4) by Stoddard & Ford [9].

$$\phi(r) = 4\varepsilon\left[\left\{\left(\frac{\sigma}{r}\right)^{12} - \left(\frac{\sigma}{r}\right)^{6}\right\} + \left(6{r_C}^{*-12} - 3{r_C}^{*-6}\right)\left(\frac{r}{r_C}\right)^2 - \left(7{r_C}^{*-12} - 4{r_C}^{*-6}\right)\right] \quad (4)$$

2.2.2 Effective pair potential for water. The effective pair potential form for liquid water has been intensively studied. The classical ST2 potential proposed in 1974 by Stillinger and Rahman [10] based on BNS model [11] was widely used in the 1980s. The rigid water molecule was modeled as Fig. 2a, with the distance of OH just 0.1 nm and the angle of HOH the tetrahedral angle $\theta_t = 2\cos^{-1}\left(1/\sqrt{3}\right) \cong$ 109.47°. Point charges at four sites shown in Fig. 2a were assumed: positive charge of 0.235 7 e each on hydrogen sites and two negative charges at positions of lone electron pairs (tetrahedral directions). They modeled the potential function as the summation of Coulomb potential between charges and the Lennard-Jones potential between oxygen atoms. Hence, the effective pair potential of molecules at $\boldsymbol{R}_1$ and $\boldsymbol{R}_2$ are expressed as

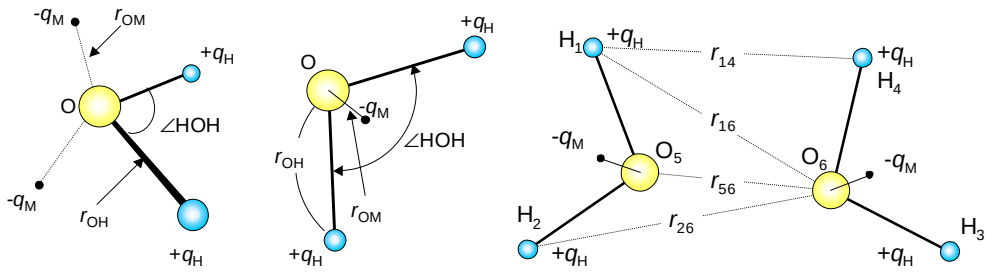

Figure 2 Water potential structures for (a) 5 sites model, ST2, (b) 4 sites and 3 sites models, TIP4P, CC, SPC, SPC/E, (c) definition of interatomic length of MCY and CC potential.

Table 3 Potential parameters for water.

		ST2	SPC/E	TIP4P	CC
r_{OH}	[nm]	0.100	0.100	0.095 72	0.095 72
∠HOH	[°]	109.47	109.47	104.52	104.52
σ_{OO}	[nm]	0.310	0.316 6	0.315 4	N/A
ε_{OO} $\times 10^{-21}$	[J]	0.526 05	1.079 7	1.077 2	N/A
r_{OM}	[nm]	0.08	0	0.015	0.024 994
q_H[a]	[C]	0.235 7 *e*	0.423 8 *e*	0.52 *e*	0.185 59 *e*
q_M	[C]	-0.235 7 *e*	-0.847 6 *e*	-1.04 *e*	-0.371 18 *e*

[a]Charge of electron $e = 1.60219\times10^{-19}$ C

$$\phi_{12}(\boldsymbol{R}_1, \boldsymbol{R}_2) = 4\varepsilon_{OO}\left[\left(\frac{\sigma_{OO}}{R_{12}}\right)^{12} - \left(\frac{\sigma_{OO}}{R_{12}}\right)^{6}\right] + S(R_{12})\sum_i\sum_j \frac{q_i q_j}{4\pi\varepsilon_0 r_{ij}}, \qquad (5)$$

where R_{12} represents the distance of oxygen atoms, and σ_{OO} and ε_{OO} are Lennard-Jones parameters. The Coulombic interaction is the sum of 16 pairs of point charges. $S(R_{12})$ is the modulation function to reduce the Coulombic force when two molecules are very close.

Later, much simpler forms of SPC (Simple Point Charge) [12] and SPC/E (Extended SPC) [13] potentials were introduced by Berendsen *et al.* SPC/E potential employed the configuration in Fig. 2b, with charges on oxygen and hydrogen equal to –0.8476 and +0.4238 *e*, respectively. Lennard-Jones function of oxygen-oxygen interaction was used as ST2 as in Eq. (5) but without the modulation function $S(R_{12})$.

TIP4P potential proposed by Jorgensen *et al*. [14] employed the structure of water molecule as r_{OH} = 0.09572 nm and ∠HOH = 104.52° based on the experimentally assigned value for the isolated molecule. The positive point charges *q* were on hydrogen atoms, and the negative charge –2*q* was set at r_{OM} from the oxygen atom on the bisector of the HOH angle, as in Fig. 2b. The function can be written as Eq. (5) without $S(R_{12})$ function. The parameters listed in Table 3 were optimized for thermodynamic data such as density, potential energy, specific heat, evaporation energy, self-diffusion coefficient and thermal conductivity, and structure data such as the radial distribution function and neutron diffraction results at 25 °C and 1atm. This potential is regarded as one of the OPLS (optimized potential for liquid simulations) set covering liquid alcohols and other molecules with hydroxyl groups developed by Jorgensen [15].

MYC potential [16] and CC potential [17] were based on *ab initio* quantum molecular calculations of water dimer with the elaborate treatment of electron correlation energy. The assumed structure and the distribution of charges are the same as TIP4P as shown in Fig. 2b with a different length r_{OM} and amount of charge as in Table 3. For CC potential, the interaction of molecules is parameterized as follows.

$$\phi_{12}(\boldsymbol{R}_1, \boldsymbol{R}_2) = \sum_i \sum_j \frac{q_i q_j}{4\pi\varepsilon_0 r_{ij}} + a_1 \exp(-b_1 r_{56}) + a_2\left[\exp(-b_2 r_{13}) + \exp(-b_2 r_{14}) + \exp(-b_2 r_{23}) + \exp(-b_2 r_{24})\right] + a_3\left[\exp(-b_3 r_{16}) + \exp(-b_3 r_{26}) + \exp(-b_3 r_{35}) + \exp(-b_3 r_{45})\right] - a_4\left[\exp(-b_4 r_{16}) + \exp(-b_4 r_{26}) + \exp(-b_4 r_{35}) + \exp(-b_4 r_{45})\right] \quad (6)$$

$a_1 =$ 315.708 $\times 10^{-17}$ [J], $b_1 =$ 47.555 [1/nm],
$a_2 =$ 2.4873 $\times 10^{-17}$ [J], $b_2 =$ 38.446 [1/nm],
$a_3 =$ 1.4694 $\times 10^{-17}$ [J], $b_3 =$ 31.763 [1/nm],
$a_4 =$ 0.3181 $\times 10^{-17}$ [J], $b_4 =$ 24.806 [1/nm].

Among these rigid water models, SPC/E, TIP4P and CC potentials are well accepted in recent simulations of liquid water such as the demonstration of the excellent agreement of surface tension with experimental results using SPC/E potential [18]. Because all of these rigid water models are "effective" pair potential optimized for liquid water, it must be always questioned if these are applicable to small clusters, wider range of thermodynamics condition, or liquid-vapor interface. Even though the experimental permanent dipole moment of isolated water is 1.85 D[1], most rigid models employ higher value such as 2.351 D for SPC/E to effectively model the induced dipole moment at liquid phase. The direct inclusion of the polarizability to the water models results in the many-body potential, which requires the iterative calculation of polarization depending on surrounding molecules. The polarizable potential based on TIP4P [19], MCY [20] and SPC [21] are used to simulate the structure of small clusters and transition of monomer to bulk properties. On the other hand, flexible water models with spring [22] or Morse type [23] intramolecular potential are examined seeking for the demonstration of vibrational spectrum shift and for the reasonable prediction of dielectric constant.

2.2.3 Many-body potential for carbon and silicon. The approximation of pair potential cannot be applied for atoms with covalent chemical bond such as silicon and carbon. SW potential for silicon proposed by Stillinger and Weber in 1985 [24] was made of two-body term and three-body term that stabilize the diamond structure of silicon. Tersoff [25, 26] proposed a many-body potential function for silicon, carbon, germanium and combinations of these atoms. For simulations of solid silicon, this potential [26] is widely used. Brenner modified the Tersoff potential for carbon and extended it for a hydrocarbon system [28]. A simplified form of Brenner potential removing rather complicated 'conjugate terms' is widely used for studies of fullerene [29, 30] and carbon-nanotube. Both Tersoff potential and the simplified Brenner potential can be expressed as following in a unified form. The total potential energy of a system is expressed as the sum of every chemical bond as

[1] 1 D = 3.3357×10^{-30} Cm in SI unit.

$$\Phi = \sum_i \sum_{j(i<j)} f_{\mathrm{C}}(r_{ij})\left\{V_{\mathrm{R}}(r_{ij}) - b^*{}_{ij} V_{\mathrm{A}}(r_{ij})\right\}, \tag{7}$$

where the summation is for every chemical bond. $V_{\mathrm{R}}(r)$ and $V_{\mathrm{A}}(r)$ are repulsive and attractive parts of the Morse type potential, respectively.

$$V_{\mathrm{R}}(r) = f_{\mathrm{C}}(r)\frac{D_{\mathrm{e}}}{S-1}\exp\left\{-\beta\sqrt{2S}\left(r - R_{\mathrm{e}}\right)\right\} \tag{8}$$

$$V_{\mathrm{A}}(r) = f_{\mathrm{C}}(r)\frac{D_{\mathrm{e}}S}{S-1}\exp\left\{-\beta\sqrt{2/S}\left(r - R_{\mathrm{e}}\right)\right\} \tag{9}$$

The cutoff function $f_{\mathrm{C}}(r)$ is a simple decaying function centered at $r = R$ with the half width of D.

$$f_{\mathrm{C}}(r) = \begin{cases} 1 & (r < R - D) \\ \dfrac{1}{2} - \dfrac{1}{2}\sin\left[\dfrac{\pi}{2}(r - R)/D\right] & (R - D < r < R + D) \\ 0 & (r > R + D) \end{cases} \tag{10}$$

Finally, $b^*{}_{ij}$ term expresses the modification of the attractive force $V_{\mathrm{A}}(r)$ depending on θ_{ijk}, the bond angle between bonds i-j and i-k.

$$b^*{}_{ij} = \frac{b_{ij} + b_{ji}}{2}, \quad b_{ij} = \left(1 + a^n\left\{\sum_{k(\neq i,j)} f_C(r_{ik})g(\theta_{ijk})\right\}^n\right)^{-\delta} \tag{11}$$

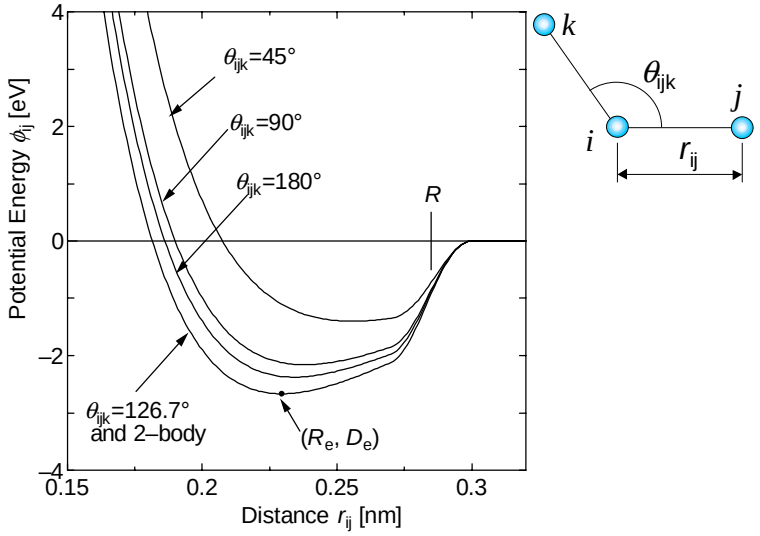

Figure 3 Many-body characteristics of Tersoff potential for silicon.

Table 4 Parameters for Tersoff potential and Brenner potential.

	Tersoff (Si)	Tersoff (C)	Brenner (C)
D_e [eV]	2.6660	5.1644	6.325
R_e [nm]	0.2295	0.1447	0.1315
S	1.4316	1.5769	1.29
β [nm^{-1}]	14.656	19.640	1.5
A	1.1000×10^{-6}	1.5724×10^{-7}	1.1304×10^{-2}
N	7.8734×10^{-1}	7.2751×10^{-1}	1
δ	$1/(2n)$	$1/(2n)$	0.80469
C	1.0039×10^{5}	3.8049×10^{4}	19
D	1.6217×10^{1}	4.384	2.5
H	-5.9825×10^{-1}	-5.7058×10^{-1}	-1
R [nm]	0.285	0.195	0.185
D [nm]	0.015	0.015	0.015

$$g(\theta) = 1 + \frac{c^2}{d^2} - \frac{c^2}{d^2 + (h - \cos\theta)^2} \tag{12}$$

Parameter constants for Tersoff potential for silicon (improved elastic properties) [26] and carbon and Brenner potential for carbon are listed in Table 4. In order to illustrate the characteristic of Tersoff and Brenner potential function, a potential energy contribution from a bond is expressed in Fig. 3. The Tersoff parameters for silicon are assumed and the energy of *i-j* bond under the influence of the third atom *k*, $\phi' = f_C(r_{ij})\{V_R(r_{ij}) - b_{ij}V_A(r_{ij})\}$ is drawn. The effect of the third atom *k* is negligible only when the angle θ_{ijk} is 126.7°.

2.3 Integration of the Newtonian Equation

The integration of the equation of motion is straightforward. Unlike the simulation of fluid dynamics, simpler integration scheme is usually preferred [5]. Verlet's integration scheme, as follows, can be simply derived by the Taylor series expansion of the equation of motion.

$$\boldsymbol{r}_i(t + \Delta t) = 2\boldsymbol{r}_i(t) - \boldsymbol{r}_i(t - \Delta t) + (\Delta t)^2 \boldsymbol{F}_i(t)/m_i \tag{13}$$

$$\boldsymbol{v}_i(t) = \{\boldsymbol{r}_i(t + \Delta t) - \boldsymbol{r}_i(t - \Delta t)\}/2\Delta t \tag{14}$$

where Δt is the time step. A bit modified leap-frog method, as follows, is widely used in practical simulations [5]. After the velocity of each molecule is calculated

as Eq. (15), the position is calculated as Eq. (16).

$$\mathbf{v}_i\left(t+\frac{\Delta t}{2}\right)=\mathbf{v}_i\left(t-\frac{\Delta t}{2}\right)+\Delta t\frac{\mathbf{F}_i(t)}{m_i} \tag{15}$$

$$\boldsymbol{r}_i(t+\Delta t)=\boldsymbol{r}_i(t)+\Delta t\boldsymbol{v}_i\left(t+\frac{\Delta t}{2}\right) \tag{16}$$

Typical time step Δt is about 0.005 τ or 10 fs with argon property of Lennard-Jones potential. More elaborate integration schemes such as Gear's predictor-corrector method [5] are sometimes employed depending on the complexity of the potential function and the demand of the accuracy of motion in each time step.

2.4 Boundary Condition: Spatial and Temporal Scale

Since the spatial and temporal scale handled with the MD method is extremely small compared to the scale of macroscopic heat transfer phenomena, the most important point of the design of a MD simulation applied to the macroscopic problem is the boundary condition. Many problems in chemistry, where the reaction process in the macroscopic chamber can be described with simple chemical reaction formulas, can be simulated in a relatively small equilibrium system. This situation can be understood by noting that the energy scale of chemical reaction is much higher than the energy scale of interaction with ambient molecules. Then, the interaction with other molecules can all be included with the thermodynamic properties such as temperature and pressure. On the other hand, because most problems in heat transfer deal with the temperature itself, interaction with 'ambient' molecules is usually very important.

Many MD simulations in chemistry and statistical mechanics have used the fully periodic boundary condition, which assumes that the system is simply homogeneous for an infinite length scale. The implementation of the periodic boundary condition is very simple. Any information beyond a boundary can be calculated with the replica of molecules, as in Fig. 4. This boundary condition is

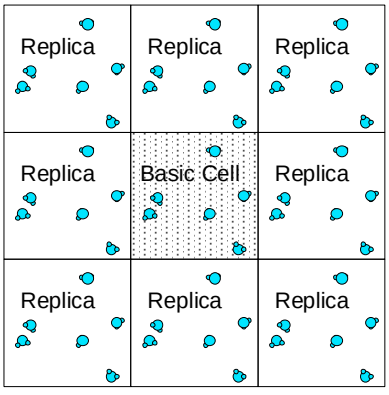

Figure 4 Periodic boundary condition.

used for two or four directions even for non-equilibrium calculations. The interaction of molecules is calculated beyond the periodic boundary with replica molecules. In order to avoid the calculation of potential between a molecule and its own replica, the potential must be cutoff to smaller than half the width of the base-cell scale. This cannot be a big problem for the short-range force such as Lennard-Jones potential, which decays as r^{-6}. Since Coulombic force decays only with r^{-1}, the simple cutoff does not give a good result. Usually, the well-known Ewald sum method [5] is employed, where the contribution from molecules in replica cells is approximated by a sophisticated manner. This is also somewhat of a problem for a system without the fully periodic conditions. The calculation of pressure using the virial theorem in Eq. (23) is also not straightforward. The sum of the potential terms in principal should be for the molecules inside the control volume *V*. However, for the fully periodic condition, the treatment of the pairs of potential as others gives a good result. For a spatially non-equilibrium situation, measurements of pressure and stress tensor are very complicated. The stress tensor defined in a surface rather than the volume as in Eq. (23) is demonstrated to be better [31, 32].

Many problems in heat transfer may include a phenomenon with a larger scale than the calculation domain, such as instability or a large modulation of properties. The temperature and specific volume condition where the phase separation happens in a macroscopic condition may be simulated as formation of the cluster in the small-scale calculation. Furthermore, for the non-equilibrium simulations, the establishment of the proper boundary condition is very difficult. In addition, the time scale that a MD simulation can handle might be too short to simulate the dynamic process. Examples of non-equilibrium systems are discussed in section 5.

The difficulty in the boundary condition is less for gas-phase molecules because the contribution of potential energy compared to kinetic energy is small. If the potential contribution is ignored, some simple boundary condition such as mirror reflection boundary can be used. Simply changing the velocity component as if a molecule makes an inelastic reflection. There is no good boundary condition for a liquid system. When it is impossible to use the periodic boundary condition, a solid wall or a vapor layer should be connected. Several different levels of the solid boundary conditions can be used. By locating an array of stationary molecules, the 0 K solid boundary can be constructed. Since the stationary molecules do not exchange the kinetic energy, they can be regarded as thermally adiabatic.

A one-dimensional potential function equivalent to the integration of the solid molecules can be used to represent an adiabatic wall. For example, the integration of a layer of fcc (111) surface of Lennard-Jones molecules can be expressed as

$$\Phi(z) = \frac{4\sqrt{3}\pi}{15} \frac{\varepsilon_{\mathrm{INT}} {\sigma_{\mathrm{INT}}}^2}{{R_0}^2} \left\{ 2\left(\frac{\sigma_{\mathrm{INT}}}{z} \right)^{10} - 5\left(\frac{\sigma_{\mathrm{INT}}}{z} \right)^{4} \right\} \tag{17}$$

where $\varepsilon_{\mathrm{INT}}$ and σ_{INT} are Lennard-Jones energy and length parameters between the solid molecule and the liquid molecule. R_0 and z are the nearest neighbor distance of solid molecules and the coordinate normal to the surface, respectively. On the other hand, the volume integral is possible by imagining as if solid molecules are a continuum.

$$\Phi(z) = \frac{2\pi}{45}\frac{\rho_{\mathrm{S}}}{m_{\mathrm{S}}}\varepsilon_{\mathrm{INT}}\sigma_{\mathrm{INT}}{}^{3}\left\{2\left(\frac{\sigma_{\mathrm{INT}}}{z}\right)^{9} - 15\left(\frac{\sigma_{\mathrm{INT}}}{z}\right)^{3}\right\} \tag{18}$$

where $\rho_{\mathrm{S}}/m_{\mathrm{S}}$ is the number density of solid.

However, most heat transfer simulations prefer to use the constant temperature solid wall. The simple velocity scaling in section 2.5 is often applied to three crystal layers of harmonic molecules. Since the velocity scaling is too artificial, the following phantom technique [33-36] is recommended. Phantom molecules model the infinitely wide bulk solid kept at a constant temperature T with the proper heat conduction characteristics. An example of the configuration of phantom molecules for a harmonic fcc solid system is shown in Fig. 5. A phantom molecule is connected to each molecule of the solid layer through a spring of $2k$ and a damper of $\alpha = m\omega_D\pi/6$ in the vertical direction and with springs of $3.5k$ and dampers of α in two horizontal directions. Here, ω_{D} is the Debye frequency. Each phantom molecule is excited by the random force of Gaussian distribution with the standard deviation $\sigma_{\mathrm{F}} = \sqrt{2\alpha k_{\mathrm{B}}T/\Delta t}$. The energy flux to the calculation system can be accurately calculated by integrating the exciting force and the damping force applied to phantom molecules [36].

Through the careful matching of the boundary conditions, the MD simulation can find a way to connect to statistical techniques for gas and solid, which can easily handle much larger spatial and temporal scales. Some indirect examples are modeling the collision dynamics [37, 38] or the gas-surface interaction [39] for DSMC simulations through MD simulations. Furthermore, the boundary condition of phonon dynamics should be handled by the MD method.

2.5 Initial Condition and Control of Temperature and/or Pressure

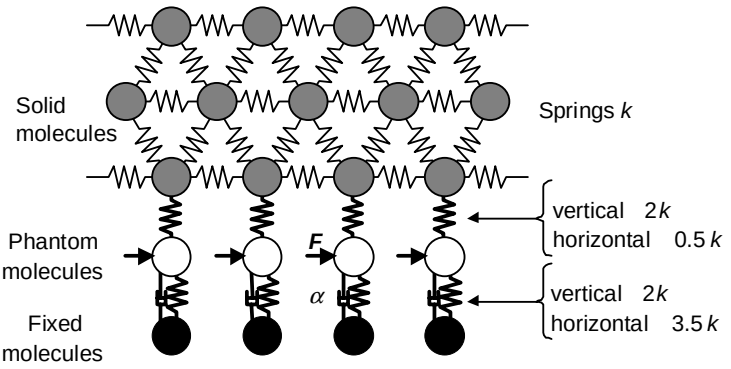

Figure 5 Constant temperature solid wall with phantom molecules.

The initial condition for each molecule is usually assigned by giving the velocity $v = \sqrt{3k_B T_C / m}$ with random directions for all molecules. The Maxwell-Boltzmann velocity distribution can be obtained after some equilibration calculations. The equilibrium system can often be calculated for constant temperature and constant pressure conditions. The simple temperature control of the equilibrium system can be realized by just scaling the velocity of molecules as $v_i' = v_i \sqrt{T / T_C}$ with the current temperature T and the desired temperature T_C. More elaborate techniques to realize the constant temperature system are known as the Anderson method [40] and the Nosé-Hoover method [41, 42].

Anderson method mimics random collisions with an imaginary heat bath particle. At intervals, the velocity of a randomly selected molecule is changed to a value chosen from the Maxwell-Boltzmann distribution. The choice of this interval is an important parameter. The Nosé-Hoover thermostat method involve the modification of the equation of motion as

$$m_i \frac{d^2 \boldsymbol{r}_i}{dt^2} = \boldsymbol{F}_i - \zeta m_i \frac{d\boldsymbol{r}_i}{dt}, \quad \frac{d\zeta}{dt} = \frac{2\left(E_k - E_k{}^0\right)}{Q} \tag{19}$$

where ζ is the friction coefficient, E_k kinetic energy of the system, $E_k{}^0$ kinetic energy corresponding to the desired temperature T_C, and Q the thermal inertia parameter. All of these constant temperature techniques have been probed to give a statistically correct canonical ensemble, but the physical meaning of velocity re-scaling is not clear.

Andersen [40] described a technique to realize the constant pressure simulation. The simulation box size V is altered similar to the action of a piston with a mass. Parrinello and Rahman [43, 44] extended this technique to change the simulation box shape as well as size for solid crystal. Berendsen proposed a very simple "pressure bath" technique for the constant pressure simulation. The system pressure obeys $dP/dt = (P_C - P)/t_P$ by scaling the box size and position of molecules by a factor $\chi^{1/3}$ for each step.

$$\boldsymbol{r}' = \chi^{1/3} \boldsymbol{r}, \quad \chi = 1 - \beta_T \frac{\Delta t}{t_p} \left(P_C - P\right) \tag{20}$$

where β_T, t_p are the isothermal compressibility and time constant parameter, respectively.

Finally, it should be stressed again that all of these techniques of constant temperature or constant pressure are artificial to reproduce the statistical ensemble, and the physical meaning of the modification of position or velocity of each molecule is not clear.

2.6 Thermophysical and Dynamic Properties

According to statistical mechanics, thermodynamics properties such as temperature, internal energy and pressure can be defined as

Temperature
$$T = \frac{1}{3Nk_{\mathrm{B}}}\left\langle \sum_{i=1}^{N} m_i v_i^{\,2} \right\rangle \tag{21}$$

Internal energy
$$U = \frac{3}{2}Nk_{\mathrm{B}}T + \left\langle \sum_i \sum_{j>i} \phi(\boldsymbol{r}_{ij}) \right\rangle \tag{22}$$

Pressure
$$P = \frac{N}{V}k_{\mathrm{B}}T - \frac{1}{3V}\left\langle \sum_i \sum_{j>i} \frac{\partial \phi}{\partial \boldsymbol{r}_{ij}} \cdot \boldsymbol{r}_{ij} \right\rangle \tag{23}$$

Here, temperature is simply the kinetic energy of molecules, and the internal energy is the total energy of kinetic and potential energies. Calculations of these properties are trivial. The pressure is defined through the virial theorem. There is no established technique to measure entropy and free energy by the MD method. These properties can be obtained by the statistical Monte Carlo method briefly discussed in section 2.7.

Some dynamics properties such as self-diffusivity, thermal conductivity and viscosity can be calculated by the equilibrium simulations though the fluctuations of properties, assuming that the macroscopic concepts of the linear equations such as Fick's law or Fourier's law are valid. The definitions of the equations, statistical mechanical Green-Kubo formula and the practical formulas derived using the Einstein relations are listed in Table 5.

The far-infrared and infrared absorption spectrum related to the radiative heat transfer can be calculated [46, 47] by employing the quantum mechanical perturbation theory. The absorption cross-section per molecule $\alpha(\omega)$ for light of frequency ω is derived as follows: Assuming that light interferes only to the permanent electric dipole moment, $\alpha(\omega)$ is expressed as

Table 5 Calculations of dynamic properties.

Property	Definition	Statistical Mechanical Green-Kubo Formula	With Einstein Relation For large *t*
Diffusion coefficient	$\dot{n} = -D\frac{\partial n}{\partial x}$	$\frac{1}{3}\int_0^\infty \langle \boldsymbol{v}_i(t)\cdot\boldsymbol{v}_i(0)\rangle dt$	$\frac{1}{6t}\left\langle \lvert \boldsymbol{r}_i(t)-\boldsymbol{r}_i(0)\rvert^2 \right\rangle$
Thermal conductivity[1]	$q = -\lambda\frac{\partial T}{\partial x}$	$\frac{V}{k_B T^2}\int_0^\infty \langle \tilde{q}_\alpha(t)\cdot\tilde{q}_\alpha(0)\rangle dt$	$\frac{V}{k_B T^2 2t}\left\langle (\delta\varepsilon_\alpha(t)-\delta\varepsilon_\alpha(0))^2 \right\rangle$
Shear viscosity[2]	$F = \mu\frac{\partial U}{\partial y}$	$\frac{V}{k_B T}\int_0^\infty \langle \tilde{p}_{\alpha\beta}(t)\cdot\tilde{p}_{\alpha\beta}(0)\rangle dt$	$\frac{V}{k_B T 2t}\left\langle \left(\tilde{D}_{\alpha\beta}(t)-\tilde{D}_{\alpha\beta}(0)\right)^2 \right\rangle$

1. $\tilde{q}_\alpha = \frac{\mathrm{d}\delta\varepsilon_\alpha}{\mathrm{d}t}$, $\delta\varepsilon_\alpha = \frac{1}{V}\sum_i r_{i\alpha}(\varepsilon_i - \langle\varepsilon_i\rangle)$, $\varepsilon_i = \frac{m_i v_i^{\,2}}{2} + \frac{1}{2}\sum_{j\neq i}\phi(r_{ij})$, $\alpha = x, y, z$

2. NVE only. $\tilde{p}_{\alpha\beta} = \frac{1}{V}\left(\sum_i m_i v_{i\alpha} v_{i\beta} + \sum_i\sum_{j>i} r_{ij\alpha} f_{ij\beta}\right)$, $\tilde{D}_{\alpha\beta} = \frac{1}{V}\sum_i m_i r_{i\alpha} v_{i\beta}$, $\alpha\beta = xy, yz, zx$

$$\alpha(\omega) = \frac{\pi\omega\{1-\exp(-\hbar\omega/k_{\mathrm{B}}T)\}}{3\varepsilon_0\hbar ncN} I(\omega), \tag{24}$$

$$I(\omega) = \frac{1}{2\pi}\int_{-\infty}^{\infty} \exp(-i\omega t)\mathrm{d}t\left\langle \boldsymbol{\mu}(0)\cdot\boldsymbol{\mu}(t)\right\rangle_0 \tag{25}$$

where c and n are the speed of light and the refractive index, which is often assumed to be unity, respectively. $I(\omega)$ and $\boldsymbol{\mu}(t)$ are the transition rate and the electric dipole moment, respectively. The ensemble average $\left\langle \boldsymbol{\mu}(0)\cdot\boldsymbol{\mu}(t)\right\rangle_0$ is equivalent to the autocorrelation, and $I(\omega)$ reduces to the power spectrum of the electric dipole moment of the system. For the classical equilibrium system, the absorption cross section tends to the following equation as the classical limit of $\hbar\omega/k_{\mathrm{B}}T \to 0$.

$$\alpha(\omega) = \frac{\pi\omega^2}{3\varepsilon_0 k_{\mathrm{B}}TncN} I(\omega) \tag{26}$$

2.7 Monte Carlo Simulation

The Monte Carlo (MC) method or Metropolis method is often compared to the MD method. With the MC method, the same potential function as MD can be used. Instead of propagating positions of molecules based on the equation of motion in Eq. (1), configurations of molecules are generated with random numbers so that the probability of a configuration is proportional to the statistical probability for the ensemble considered. For example, the configuration should obey the Boltzmann distribution for a constant NVT (number, volume and temperature: canonical) ensemble. After generating such molecular configurations, the average value of any physical property can be obtained as a weighted integral of the configurations. The MC method has an advantage compared with MD when a physical property for a statistical ensemble is calculated. The MC method is established for constant NVE (number, volume and energy: microcanonical), constant NVT (number, volume and temperature: canonical), constant NPT (number, pressure and temperature), and even constant μVT (chemical potential, volume and temperature: grand-canonical) ensembles. However, the dynamic properties such as diffusivity or viscosity cannot be calculated by the statistical MC method. Furthermore, the non-equilibrium system such as the system with heat flux cannot be handled with the MC method.

3 LIQUID-VAPOR INTERFACE

3.1 Surface Tension

Surface tension is one of the benchmark properties to examine the applicability of a potential function to the liquid-vapor interface. Figure 6 shows an example of liquid-vapor interfaces of liquid slab [48, 49]. The calculation region had periodic

boundary conditions for all six boundaries. Starting from a crystal of argon continuing over side boundaries, the liquid slab with flat liquid-vapor interface in Fig. 6 was realized after 2 ns MD simulation. Considering the periodic boundary conditions, this liquid slab can be regarded as an infinitely wide thin liquid film. During the simulation, the number of molecules, volume and total energy of the system were conserved except for the early temperature control period. When the liquid layer is thick enough, the bulk property of liquid can be obtained at the central region, and two liquid-vapor interfaces can be realized. The vapor (open), interfacial (gray), and liquid (solid) molecules are distinguished by the potential felt by each molecule. By taking a time average, the density profile in Fig. 6b, pressure tensor, and surface tension can be reasonably predicted. This is the typical molecular configuration for the measurement of surface tension. The quite accurate prediction of surface tension has been demonstrated for Lennard-Jones fluid [8] and water [18] by integrating the difference of normal $P_N(z)$ and tangential $P_T(z)$ components of pressure tensor across the surface as

$$\gamma_{LG} = \int_{z_L}^{z_G} [P_N(z) - P_T(z)] dz , \tag{27}$$

where z is the coordinate perpendicular to the interface. Here, P_N and P_T are equal to the thermodynamic pressure P in bulk vapor position z_G and bulk liquid position z_L. In the case of liquid slab as shown in Fig. 6, the integration between two vapor regions results in $2\gamma_{LG}$ since there are two liquid-vapor interfaces. In principle, the normal pressure $P_N(z)$ should be completely constant through the

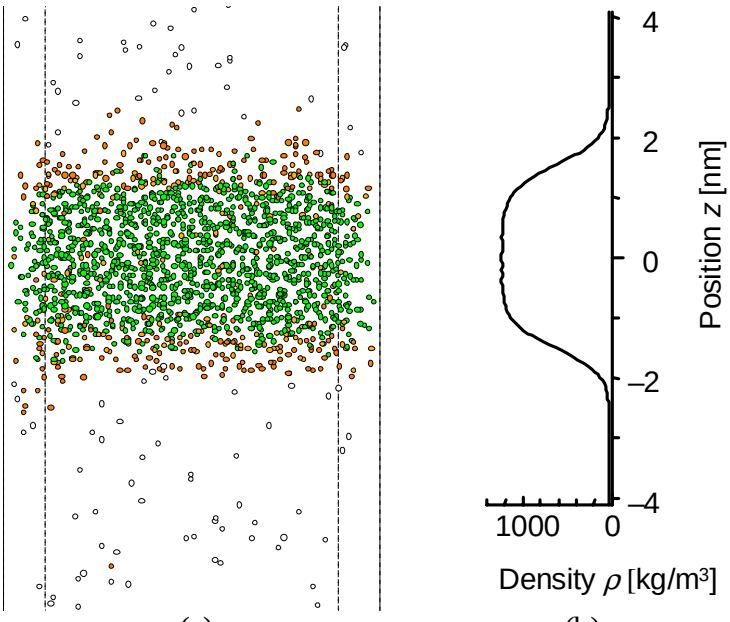

(a) (b)

Figure 6 A flat interface of liquid and vapor (1944 argon molecules saturated at 100 K in 5.5×5.5×20 nm box), (a) a snapshot, (b) density distribution.

interface for the mechanical balance required at equilibrium. The reason for integrating the pressure difference in Eq. (27) is believed to reduce the numerical fluctuations by canceling the common kinetic term of the pressure expression [the first term of Eq. (23)]. However, it seems to also cancel the problem of the pressure definition in locally non-uniform density variation across the interface [32].

3.2 Liquid Droplet and Young-Laplace Equation

Figure 7 shows examples of argon and water liquid droplet surrounded by its vapor [48, 49]. This configuration can be obtained when the initial argon crystal is placed at the center of the fully periodic cubic region. This is regarded as an isolated liquid droplet floating in its vapor. When the size of the droplet is large enough, the bulk property of liquid is expected at the central region. The well-known Young-Laplace equation relates the curvature of a liquid-vapor interface and surface tension to the pressure difference. For a liquid droplet, the Young-Laplace equation is described as

$$\gamma_{\mathrm{LG}} = \frac{(P_{\mathrm{L}} - P_{\mathrm{G}})R}{2}. \tag{28}$$

The microscopic representation of the Young-Laplace equation can be used for the evaluation of the surface tension itself, which should be a kinetic property derived from the molecular parameters. It is necessary to obtain the pressure variation across the liquid and vapor interface in order to obtain P_{L} and P_{G} as asymptotic values. The estimation of the pressure profile is quite difficult and results in a considerable error. Thompson *et al*. [50] used the following spherical extension of Irving-Kirkwood's formula to calculate the normal pressure profile:

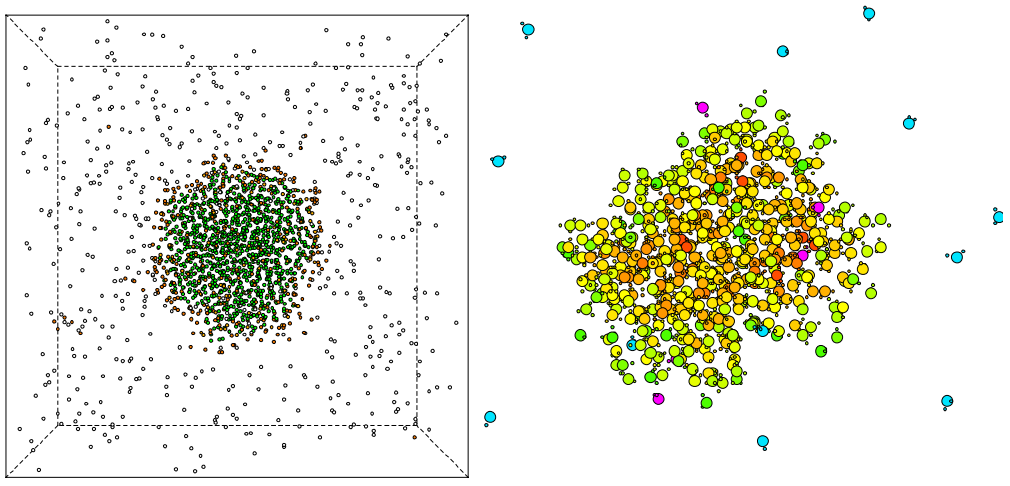

(a) (b)

Figure 7 Liquid droplet and surrounding vapor. (a) 2 048 argon molecules saturated at 95 K in a 12 nm cubic box, (b) Water droplet at 380 K.

$$P_{\mathrm{N}}(r) = k_{\mathrm{B}}T\frac{\rho(r)}{m} - \frac{1}{4\pi r^2}\sum_k f_k \tag{29}$$

$$P_{\mathrm{N}}(r) = k_{\mathrm{B}}T\frac{\rho(r)}{m} - \frac{1}{4\pi r^3}\sum_k \left|\boldsymbol{r}\cdot\boldsymbol{r}_{ij}\right|\frac{1}{r_{ij}}\frac{\mathrm{d}\phi(r_{ij})}{\mathrm{d}r_{ij}} \tag{30}$$

The normal pressure in Eq. (29) is measured as the force across the control spherical surface of radius r from the center of the droplet. The sum over k is over the normal component f_k of forces acting across the control surface between a pair of molecules i and j. The sign of f_k is defined as positive for repulsive forces and negative for attractive forces. Using the vector $\boldsymbol{r}_{ij} = \boldsymbol{r}_j - \boldsymbol{r}_i$ and the potential $\phi(r_{ij})$, the pressure is expressed as in Eq. (30).

The definition of the radius of a droplet is not straightforward, since the size of the droplet is normally very small and the liquid-vapor interface has a certain width as shown in Fig. 6b (planar surface). The equimolar dividing radius R_{e} defined as follows is a convenient choice.

$$mN = \frac{4\pi}{3}R_{\mathrm{e}}^{\,3}\rho_{\mathrm{L}} + \left\{L^3 - \frac{4\pi}{3}R_{\mathrm{e}}^{\,3}\right\}\rho_{\mathrm{G}} \tag{31}$$

where ρ_{L}, ρ_{G}, N, and L are liquid density, vapor density, number of molecules, and unit length of the cell, respectively. This R_{e} means the radius of a hypothetical sphere of uniform density ρ_{L} in a cubic cell of density ρ_{G}. However, the statistical mechanical choice of the radius is so-called surface of tension R_{S}. The first-order correction of the surface tension of a curved surface compared to that for a planar surface $\gamma_{\mathrm{LG}\infty}$ is expressed by the Tolman length δ.

$$\gamma_{\mathrm{LG}} = \gamma_{\mathrm{LG}\infty}\left(1 - \frac{2\delta}{R_{\mathrm{e}}}\right) + O\left(R_{\mathrm{e}}^{-2}\right), \tag{32}$$

where $\delta = z_{\mathrm{e}} - z_{\mathrm{S}}$ for a planar surface. Detailed statistical mechanical discussions compared with MD simulations for small droplets are found in the literature [50-53]. Roughly a thousand molecules are enough to calculate the reasonable value of the bulk surface tension for argon without this correction [49]. In the other extreme, the surface tension for very small clusters, which may be important in the nucleation theory discussed in section 5.2, should require some completely different approach, because such small cluster does not have the well-defined central liquid part assumed in the statistical mechanical discussions.

3.3 Condensation Coefficient

The determination of the condensation coefficient by MD simulations is a very fascinating task, as demonstrated in the review by Tanasawa [54]. The

condensation coefficient has been simply defined as the ratio of rates of the number of condensation molecules to incident molecules. Through the detailed studies of the liquid-vapor inter-phase phenomena of argon, water, and methanol, Matsumoto *et al.* [55-57] pointed out that this macroscopic concept couldn't be directly converted to the molecular scale concept. They calculated the condensation coefficient, for the first time, through MD simulations, and stressed the importance of the 'molecular exchange' process: a molecule condensed into the liquid phase lets another liquid molecule vaporize. By excluding those molecules from the number of condensing molecules, they had shown a good agreement with experiments at least for the equilibrium condition [58, 59]. In fact, the apparent 'self-reflection' of condensing molecules was always about 10 % regardless of molecular species. On the other hand, Tsuruta *et al.* [60] had reported a significant dependence of the trapping rate on the normal velocity of incident molecules. They seek the connection to the DSMC method for the calculation of the condensation process. Since there are significant differences in these two approaches, it appears that a new microscopic definition of the condensation coefficient may be necessary which is physically plausible and also useful for the further connection to the macroscopic theories.

Most of the studies with MD simulations have dealt with the equilibrium system of liquid and vapor, assuming that the condensation coefficient is a "coefficient" independent of supersaturating pressure or temperature. Recent experiment [61] has shown, however, a considerable dependence of the "coefficient" on supersaturation conditions. It seems that it is not easy to handle the non-equilibrium MD simulation [62] to explain these experimental results. On the other hand, according to the DSMC calculation [63] of the condensation phenomena, there is a quite thick layer where the vapor temperature varies from the liquid-vapor interface. Since the direct simulation of such a wide scale with the non-equilibrium MD method seems to be impossible, a connection of these two methods through a reasonable boundary treatment is desired.

4 SOLID-LIQUID-VAPOR INTERACTIONS

4.1 Liquid Droplet on Solid Surface

Solid-liquid-vapor interaction phenomena or simply contact phenomena of liquid to the solid surface have a very important role in phase-change heat transfer. Except for the direct contact heat transfer, most practical phase-change heat-transfer problems involve the solid surface as a heater or a condenser. The importance of the liquid wettability to the surface is apparent in a dropwise condensation, high-heat-flux boiling heat transfer and capillary liquid film evaporators. The mechanical and thermodynamic treatments of the traditional macroscopic approach had difficulty in the treatment of the line of three-phase contact. The contact line is the singular point in the macroscopic sense, since the non-slip condition of fluid dynamics, i.e. $U = V = 0$ at the surface, simply denies the movement of the contact line. The curious "monolayer liquid film" considered

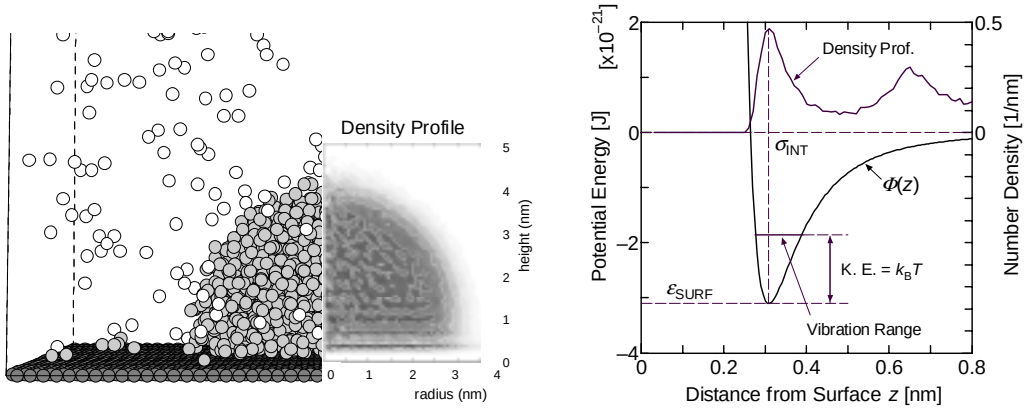

(a) (b)

Figure 8 A liquid droplet in contact with solid surface. (a) A snapshot compared with the two-dimensional density profile, (b) integrated potential profile and the density profile.

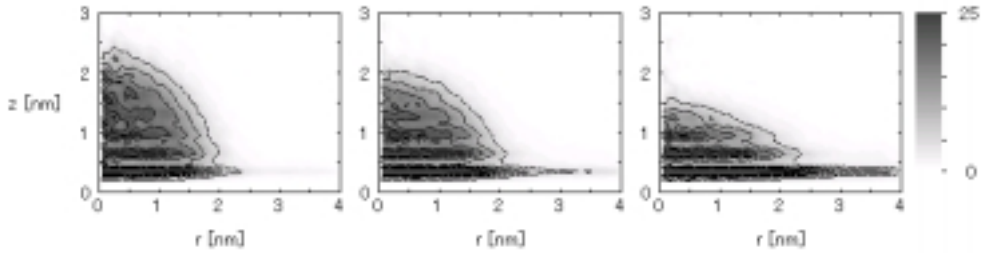

(a) (b) (c)

Figure 9 Two-dimensional density distribution of a liquid droplet on a surface for (a) E2, (b) E3, (c) E4. See Table 6 for potential parameters.

Table 6 Calculation conditions of the solid-liquid interaction.

Label	ε_{INT} [$\times 10^{-21}$J]	σ_{INT} [nm]	ε^*_{SURF}
E2	0.575	0.308 5	1.86
E3	0.750	0.308 5	2.42
E4	0.925	0.308 5	2.99

$\varepsilon^*_{SURF} = \varepsilon_{SURF} / \varepsilon_{AR}$

in some macroscopic theories of heat transfer should be examined.

There are good reviews of the connection between microscopic and macroscopic views of the wetting phenomena by Dussan [64], and from a slightly more microscopic point of view by Koplik and Banavar [65]. Figure 8a compares a snapshot of the liquid droplet in contact with a solid surface with a two-dimensional density distribution. Simulation conditions are similar to our previous reports [66, 67], but 1 944 argon molecules are included and about 1 600 molecules constitute the liquid droplet surrounded by saturated vapor. Solid molecules are located as three layers of fcc (111) surfaces with harmonic potential (only one layer is shown in Fig. 8a for simplicity). The interaction potential between argon and solid molecule expressed by the L-J potential is chosen so that the apparent contact angle becomes about 90°.

The effect of the interaction potential on the shape of the liquid droplet is

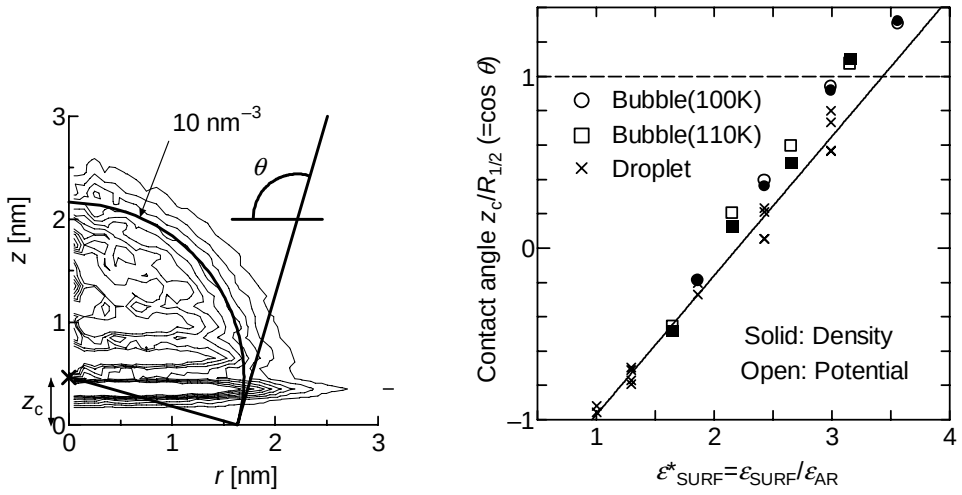

(a) (b)

Figure 10 Contact angle measured for liquid droplet and vapor bubble. (a) Definition of contact angle for liquid droplet, (b) dependence of contact angle on the integrated depth of surface potential ε_{SURF}.

apparent in Fig. 9 [66]. With increase in the strength of the interaction potential between the surface molecule and argon, the flatter shape is observed. Furthermore, with stronger interaction potential, the spread of the first layer of liquid film is much more pronounced [66]. The layered structure is commonly observed for liquid-solid interfaces and explained as due to the solvation force [68]. Figure 8b explains the reason for this layered structure more clearly. For a liquid molecule, the effect of the solid molecules can be integrated to the one-dimensional function $\Phi(z)$ in Eq. (17). This potential function is compared with the density profile in Fig. 8b. The similarity of these is remarkable, and the temperature level correlates the sharpness of the density profile. It should noticed that the integrated function Φ (z) in Eq. (17) has a minimum $\varepsilon_{SURF} = (4\sqrt{3}\pi/5)(\sigma_{INT}{}^2/R_0{}^2)\varepsilon_{INT}$ at $z = \sigma_{INT}$. The peak of the second layer of the density appears around $z = \sigma_{INT} + \sigma_{AR}$ because the second layer is trapped by the integrated potential of argon molecules layered at $z = \sigma_{INT}$.

Except for the two or three liquid layers near the surface, the averaged shape of the liquid droplet is close to the semi-spherical. In order to measure the "contact angle," we can fit a circle to a density contour disregarding the two layers of liquid near the solid surface as in Fig. 10a [66]. Controversially enough, the cosine of measured contact angle or the average shape of the droplet far from the surface was linearly dependent on the strength of the surface potential [Fig. 10b]. Comparing the simulation changing the different parameter of the interaction σ_{INT} and different configuration of the solid surface of one-dimensional function in Eq. (17), one layer of fixed molecules, three layers of harmonic molecules, the contact angle was determined by the effective integrated potential energy ε_{SURF} [66, 67].

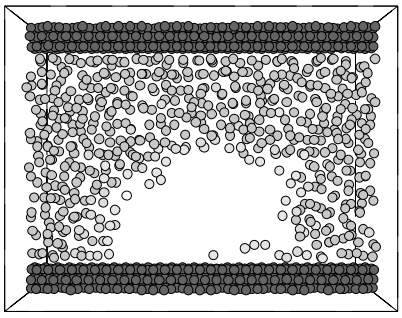

Figure 11 A snapshot of a vapor bubble (1 nm thick slice).

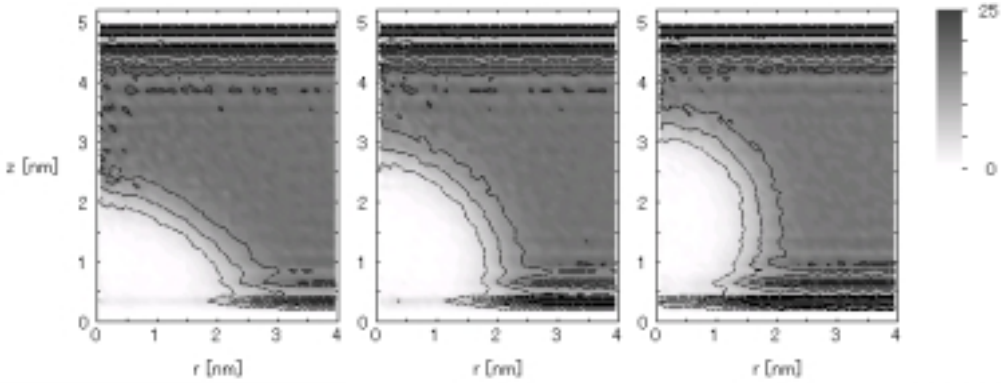

(a) (b) (c)

Figure 12 Two-dimensional density distribution of a bubble on a surface for (a) E2, (b) E3, (c) E4.

4.2 Vapor Bubble on Solid Surface

The opposite configuration of liquid and vapor, i.e. a vapor bubble in liquid, is realized for negative pressure as in Fig. 11 [35, 69]. Here, a sliced view through the center of the vapor is shown to visualize the vapor bubble in the liquid. Two dimensional density distributions for three different interaction potentials compatible to Fig. 9 are summarized in Fig. 12. The completely opposite situation of liquid and vapor is apparent, except for the layered liquid structure, which is always extending from liquid to vapor area. The contact angle measured in the same manner compared well to the liquid droplet case in Fig. 10b. The contact angle measured for the vapor bubble is slightly smaller in Fig. 10. This may be due to the effect of the surface tension on the contact line because the curvature of the contact line is opposite in two systems. One interesting point about the vapor bubble is that the first liquid layer completely covers the surface for the very wettable case of E4 in Fig. 12c. It was revealed that the $\cos\theta$ could be generalized to be $z_c/R_{1/2}$, to continuously express the dependency of the contact angle for the extremely wettable surface where z_C and $R_{1/2}$ are the center height and radius of the fitting circle (see Fig. 10a).

4.3 Contact Angle and Young's Equation

The contact angle is introduced to represent the degree of the partial wettability of the solid surface in macroscopic studies. The well-known Young's equation relates the contact angle to the balance of surface energies.

$$\cos\theta = \frac{\gamma_{SG} - \gamma_{SL}}{\gamma_{LG}}, \tag{33}$$

where γ_{SG}, γ_{SL} and γ_{LG} are surface energies between solid-vapor, solid-liquid, and liquid-vapor, respectively. This equation can be understood from the mechanical balance of forces or from the thermodynamic concept of minimizing the Helmholtz free energy. Since it is usually impossible to independently measure the surface energies except for the surface tension γ_{LG}, the well-known and useful Young's equation is still somewhat conceptual. Furthermore, the definition of the contact angle seems to be controversial if the thin liquid film exists over the 'dry' surface.

In 1977, Saville [70] claimed that the Young's equation is not satisfied from his MD results. He enclosed a liquid slab and coexisting vapor between two parallel surfaces represented by the one-dimensional potential function (Eq. (18)). Using 255 to 1205 L-J molecules at about the triplet temperature, he measured the meniscus of the liquid-vapor interface and compared it with the calculated surface tensions γ_{LG} and γ_{SL} - γ_{SG}. However, Nijmeijer *et al.* [71] showed good agreement of the observed contact angle and the contact angle calculated from Young's equation. Sikken *et al.* [72] and Nijmeijer *et al.* [71] used a little different configuration with 8500 fluid molecules and 2904 solid molecules, and the difficulty of the calculation of the surface tension term γ_{SL} - γ_{SG} was also overcome. Later, Thompson *et al.* [73] further supported the soundness of Young's equation and even discussed the dynamic contact angle. Furthermore, the contact angle measurement by the MD simulation can be useful to predict the wettability of realistic molecules on a realistic surface [74].

It seems that all these arguments and discrepancies exist not only because of the difficulties in measuring the surface energies but because the definition of the observed contact angle is not clear. As in the case of the surface tension of a droplet, a certain dividing surface of liquid-vapor must be defined to measure the contact angle. Macroscopic definition of the contact angle is valid only when the number of molecules is so large that the thickness of the interfaces is negligible. Finally, it should be noticed that the effect of the gravity is completely negligible for such a small-scale droplet. Those readers familiar with the macroscopic system should compare this system size of order of 5 nm to the capillary length.

4.4 Dynamic Process of Contact

It is well known that the measured macroscopic contact angle is a function of the velocity of the contact line U. When the contact line is moving from the liquid to vapor direction ($U > 0$), it is called advancing condition. And, the opposite ($U < 0$) is called receding condition. It is very interesting that the limit of $U = 0$ for

advancing conditions (called advancing contact angle) and that for receding conditions (receding contact angle) do not coincide. The contact angle remembers its moving history called contact angle hysteresis. From extensive macroscopic studies, it is believed that the dynamics contact angle shows the range of angles between advancing and receding due to the metastable contact directly related to the surface conditions such as roughness and chemical heterogeneity. On the other hand, there are reports of MD simulations [65, 73] that claim the reproduction of the dynamic contact angle, even though the surface is perfectly smooth and chemically homogeneous. This contradiction is still open question. It is likely to be simply that the system size of MD simulations is too small so that the crystal of solid molecules may be felt as the periodically rough potential field.

When the contact-line speed is increased for advancing conditions, the dynamic contact angle generally increases until it finally reaches 180°. Further increase in the advancing speed beyond this critical speed induces a macroscopic saw-tooth instability of the contact line. It seems that the shape of the contact line is adjusted so that the velocity component normal to the curved contact line is kept at the critical speed. Such instability cannot be reproduced in the small system used in the MD simulations. If such an extreme condition is applied to the small molecular system, probably a new instability will be induced, which is not corresponding to any macroscopic phenomena.

5. NON-EQUILIBRIUM SIMULATIONS

Heat transfer is a non-equilibrium phenomenon. Even though the thermophysical properties and inter-phase dynamics discussed in previous sections are useful for heat transfer analysis, the direct simulation of the heat transfer problem is much more desired. Here, a spatial non-equilibrium simulation refers to the system with spatial temperature gradient or heat flux. On the other hand, a temporal non-equilibrium simulation refers to the system with the temporal evolution of temperature, internal energy or other properties. Certain phenomena inherent to small scale can be studied in such a technique. On the other hand, it is not easy to extend to the macroscopic scale phenomena since the scale in the non-equilibrium direction is very small, such as the thickness in the spatially non-equilibrium system and the simulation time in temporally non-equilibrium systems. Then, the gradient of non-equilibrium is extremely large such as large heat flux and large supersaturation rate. As a typical example, the melting process seems to be easily reproduced, but the solidification process that involves the considerable ordering of molecule structure is far more difficult.

5.1 Spatially Non-Equilibrium Simulation

The thermal conductivity can be calculated with the equilibrium MD by the statistical formula in Table 5. However, the validity of Fourier's law in an extremely microscopic system such as thin film can only be examined by the direct non-equilibrium heat conduction calculation. The mechanism of heat

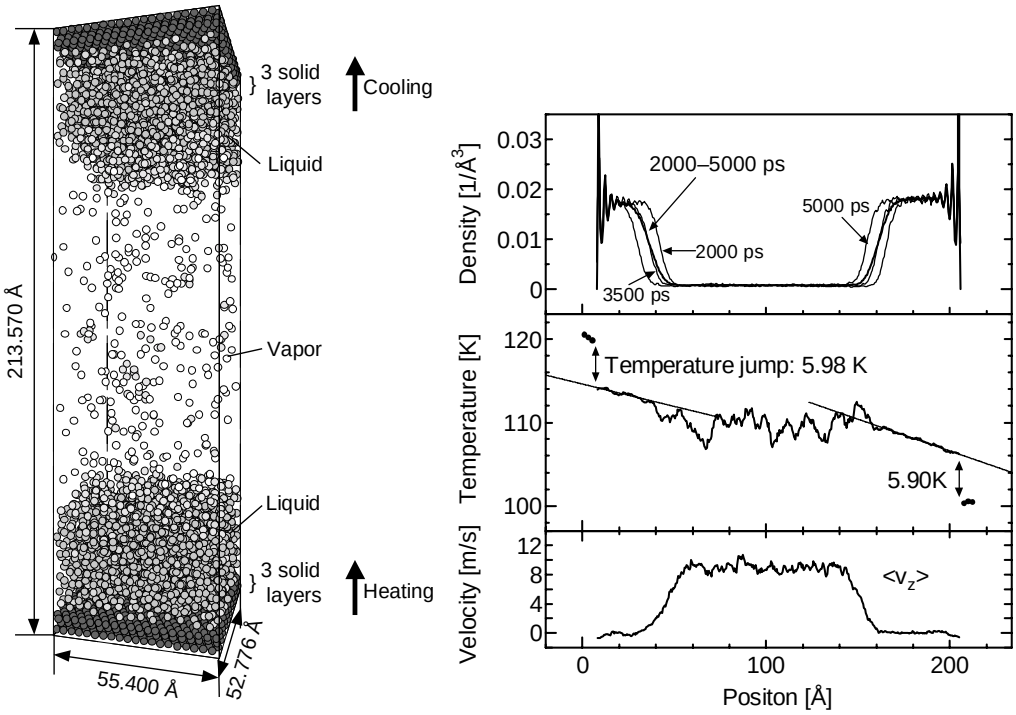

(a) (b)

Figure 13 Non-equilibrium MD for inter-phase heat transfer. (a) A snapshot, (b) density, temperature, and velocity distributions.

conduction itself is also interesting [75, 76, 77]. The heat flux through a volume is calculated as

$$\boldsymbol{q} = \frac{1}{2V}\left[\sum_{i}^{N} m_i v_i{}^2 \boldsymbol{v}_i + \sum_{i}^{N}\sum_{j\neq i}^{N} \phi_{ij}\boldsymbol{v}_i - \sum_{i}^{N}\sum_{j\neq i}^{N} \left(\boldsymbol{r}_{ij}\,\boldsymbol{f}_{ij}\right)\boldsymbol{v}_i\right] \tag{34}$$

where the first and second terms related to summations of kinetic and potential energy carried by a molecule *i*. The third term, the tensor product of vectors $\boldsymbol{r}_{ij}$ and $\boldsymbol{f}_{ij}$, represents the energy transfer by the pressure work. Because of the third term, the calculation of heat flux is not trivial at all [32].

An example of the spatial non-equilibrium simulation is shown in Fig. 13 [36]. The purpose of this simulation was to measure the thermal resistance in the interface of liquid and solid. A vapor region was sandwiched between liquid layers, which were in contact with two solid walls. While independently controlling temperatures at ends of walls by the phantom method described in section 2.5, energy flux through the system was accurately calculated. The heat flux and vapor pressure became almost constant after about 2 ns after suddenly enforcing the temperature difference between surfaces. The measured temperature distribution normal to interfaces in this quasi-steady condition shown in Fig. 13b revealed a distinctive temperature jump near the solid-liquid interface, which could be regarded as the thermal resistance over the interface. The temperature

distribution in the liquid region (see the density profile in the top panel of Fig. 13b) can be fit to a linear line, and the heat conductivity λ_L can be calculated from this gradient and heat flux q_W as $\lambda_L = q_W /(\partial T / \partial z)$. This value was actually in good agreement with the macroscopic value of liquid argon. The thermal resistance R_T was determined from the temperature jump T_{JUMP} and the heat flux q_W as $R_T = T_{JUMP} / q_W$. This thermal resistance is equivalent to 5~20 nm thickness of liquid heat conduction layer, and hence, is important only for such a small system.

The configuration in Fig. 13a seems to be used for the non-equilibrium condensation and evaporation studies since the condensation in the upper liquid-vapor interface and the evaporation in the lower interface are quasi-steady. The heat flux through higher temperature side q_W^{evap} was consumed for the latent heat of the evaporation, and the residual heat flux q_V was mostly carried by the net mass flux through the vapor region. The latent heat of condensation was added to q_V to reproduce q_W^{cond} at the lower temperature side. The measured value of heat flux q_V was about 1/3 of q_W. Then, the temperature gradient in the vapor phase is too small for the vapor heat conduction. It was revealed that the dominant carrier of energy in the vapor region was the net velocity component $<v_z>$ shown in the bottom panel of Fig. 13b. It should be noticed that when the vaporization coefficient or condensation coefficient is considered for a non-equilibrium liquid-vapor interface, the effect of this net mass flux must be removed. It seems that a considerably large vapor region should be necessary to simplify the calculation.

5.2 Homogeneous Nucleation

The homogeneous nucleation is one of the typical macroscopic phenomena directly affected by the molecular scale dynamics. Recently, Yasuoka and

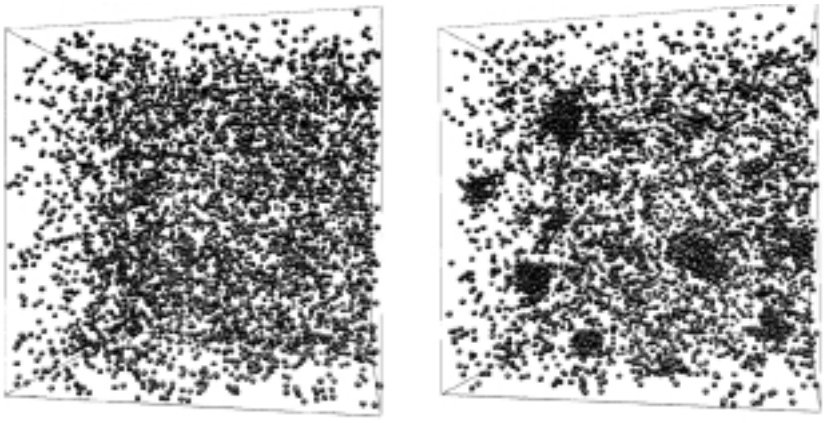

(a) (b)

Figure 14 Homogeneous nucleation of liquid droplets in L-J system by Yasuoka and Matsumoto [78], (a) after quenched: t=0, (b) at t = 600τ (1.29 ns for argon). [Reprinted from [78] by permission from Journal of Chemical Physics, copyright 1999, American Institute of Physics]

Matsumoto have demonstrated the non-equilibrium MD simulations of the nucleation process for Lennard-Jones [78] and for water [79, 80]. For the Lennard-Jones (argon) fluid, homogeneous nucleation at the triple-point temperature under supersaturation ratio of 6.8 was simulated. Snapshots of the nucleation of argon droplets are shown in Fig. 14 [78]. The appearance of several large liquid droplets is clearly observed in Fig. 14b. The key technique for such a calculation is the temperature control. After quenching to the supersaturation condition, the condensation latent heat must be removed for the successive condensation. They used 5 000 Lennard-Jones molecules for the simulation mixed with 5 000 soft-core carrier gas molecules connected to the Nosé-Hoover thermostat for the cooling agent. This cooling method mimicked the carrier gas of supersonic jet experiments. Through the detailed study of growth and delay of nuclei size distribution, they have estimated the nucleation rate and the critical size of nucleus. The nucleation rate was seven orders of magnitude larger than the prediction of classical nucleation theory, whereas the critical nucleus size was 30-40 atoms compared to 25.4 by the theory. The free energy of the formation was estimated to explain this quick nucleation. They have performed the similar simulation [79] for water of TIP4P potential at 350 K under supersaturation ratio 7.3. The calculated nucleation rate was two orders of magnitude smaller than the classical nucleation theory, just in good agreement with the "pulse expansion chamber" experimental results [81]. The estimated critical nucleus size was 30-40 compared to the prediction of classical theory of order of one.

Ikeshoji *et al.* [82, 83] have simulated the similar nucleation process of Lennard-Jones molecules with special attention to the magic number clusters of 13, 19 and 23, which are abundantly observed in experimental mass spectra. By their large-scale simulation using 65 526 molecules, the importance of the temperature control method was stressed. The Nosé-Hoover thermostat (see section 2.5) did not reproduce the magic-number clusters because the internal energy (rotation and vibration) and the translational energy decreased at almost the same rate. They introduced a special temperature control that should give a similar effect to that of Yasuoka and Matsumoto [78]. Furthermore, it was suggested that the long-time evaporation process was essential for the reproduction of the magic number clusters. Their simulation time for the evaporation process extended to 26.4 ns (argon) compared to 3.9 ns by Yasuoka and Matsumoto [78].

A MD simulation of homogeneous nucleation of a vapor bubble is much more difficult compared to the nucleation of a liquid droplet. Kinjo and Matsumoto [84] expanded a Lennard-Jones liquid to demonstrate the cavitation in negative pressure. A single cavity was formed at the thermodynamic condition near the spinodal line. Since the generation of a bubble considerably alters the system pressure of liquid, only the inception of the cavity can be studied in such a numerical system. They have roughly estimated the nucleation rate as eight orders of magnitude larger than that of the classical nucleation theory.

5.3 Heterogeneous Nucleation

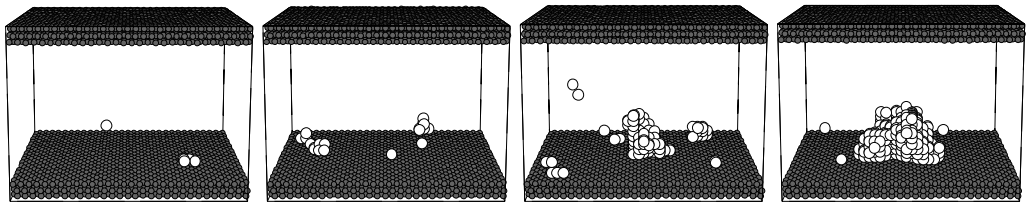

(a) (b) (c) (d)

Figure 15 Nucleation of a vapor bubble on a solid surface (E3) at (a)1.42 ns, (b)1.48 ns, (c)1.54 ns, (d)1.60 ns.

The heterogeneous nucleation is more practically important than the homogeneous nucleation in most heat transfer problems. Figure 15 shows an example of the heterogeneous nucleation of vapor bubble on a solid surface [35, 69]. Liquid argon between parallel solid surfaces was gradually expanded until a vapor bubble was nucleated. 5 488 Lennard-Jones molecules represented argon liquid, and three layers of harmonic molecules represented each solid surface with the phantom constant-temperature model in section 2.4. In order to visualize the density variations leading to the vapor bubble nucleation, three-dimensional grid points of 0.2 nm intervals were visualized as 'void' when there were no molecules within $1.2\sigma_{AR}$. The interaction potential between a solid molecule and argon was also expressed by the Lennard-Jones potential with the potential parameters σ_{INT} and $\varepsilon_{\mathrm{INT}}$. The solid-argon potential parameter was moderately wettable for the bottom surface and very wettable for the top surface. As a result, the cavity nuclei appeared and disappeared randomly on the bottom surface, and at some point they grew to a certain stable size. The calculation of the nucleation rate is not easy, as in the case of homogeneous nucleation of vapor.

5.4 Formation of Structure

The formation of a certain structure of a cluster is important even for an equilibrium case such as the supercritical condition [85], or the hydrogen-bonded

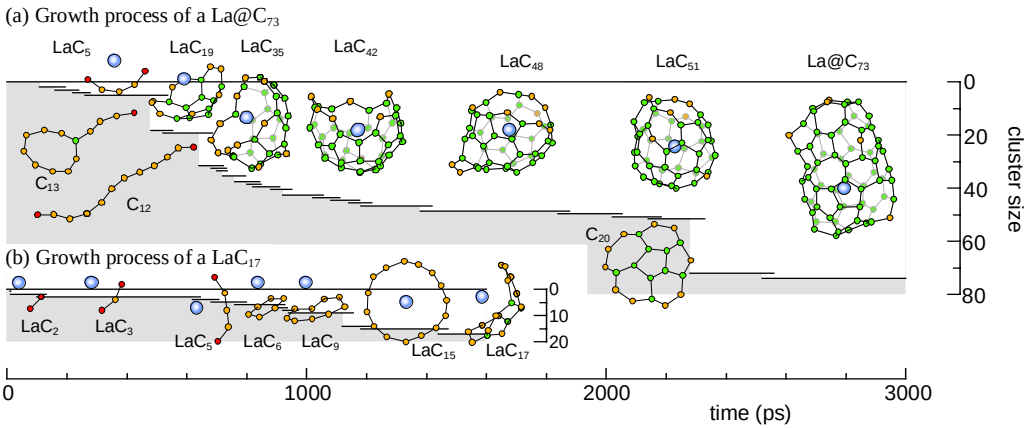

Figure 16 Growth process of La attached clusters: (a) La@C_{73} and (b) La@C_{17}.

cluster of water [86]. On the other hand, the simulation of the formation process of a special molecule structure such as fullerene [29, 30], metal-containing fullerene [87] or clathrate-hydrate [88] is very attractive. Figure 16 shows the formation process of metal (La) containing fullerene simulated by the MD method with the Brenner potential described in section 2.2.3. In addition to the Brenner potential for carbon-carbon interaction, the metal-carbon and metal-metal interaction was constructed [87] by fitting to *ab initio* calculations based on DFT (density functional theory). Since there was considerable charge transfer from the metal atom to carbon cluster, the Coulombic interaction force was included in the potential. Mainly because of this force, the metal atom works as a nucleation site for carbon clusters, as in Fig. 16. The organized clustering process of carbon cage was considerably different from the pure carbon simulation [29, 30]. This simulation is regarded as the nucleation and condensation of a carbon and metal binary mixture. As other nucleation simulations, the time scale of the simulation was compressed about 1000 times. Then the artificial temperature control was enforced to translational, rotational, and vibrational motions of freedom independently. In order to obtain the more realistic structure of C_{60} and C_{70}, the extra annealing calculations for such clusters were necessary. The multi-scale problem is much more severe in this case than in cases of argon or water, because the energy scale of chemical reaction is much higher.

6. FUTURE DIRECTIONS

The sound understanding of molecular level phenomena is required in varieties of phase-change theories such as nucleation of dropwise condensation, atomization, homogeneous and heterogeneous nucleation of vapor bubbles in cavitation and boiling. Moreover, heat transfer right at the three-phase interface, which is a singular point in the macroscopic sense, should be considered for evaporation in a micro-channel and for the micro- and macro-layer of boiling. The upper limit of heat flux of phase change must be clarified since recent advanced technologies such as intense laser light or electron beam easily achieve a very high heat flux. Phase-change phenomena involved in the thin film manufacturing process and laser manufacturing are often out of the range of the conventional approach. Other examples are surfactant effect in liquid-vapor interface and surface treatment effect of a solid surface.

Even though the MD method is a powerful tool, the reader should notice its shortcomings that the spatial and temporal scale of the system that can be handled is usually too small to directly compare with the macroscopic phenomena. Even with the rapid advances of computer technology in future, most macroscopic problems cannot be handled by directly solving each motion of molecules. Then, the ensemble technique of the molecular motion and the treatment of boundary condition must be improved for the connection to macroscopic phenomena.

Moreover, the determination of the potential function for molecules in real applications is not straightforward, and the assumption of classical potential fails when the effect of electrons is not confined in the potential form. For example,

heat conduction in metals cannot be easily handled due to free electrons. Chemical reaction processes are also difficult to handle with the classical potential. The quantum feature of electrons must be considered when electrons are excited by laser light, by electromagnetic wave or by certain chemical reactions. We encounter these problems in thin-film production and treatment processes such as CVD or plasma etching or new manufacturing techniques utilizing plasma, laser beam, and electron beam. In such processes, many heat transfer problems may be linked to higher energy phenomena than the chemical reaction. Recently, the applicability of the quantum MD method is being explored. The well-known Car-Parrinello method [89] solves the positions of atoms and electronic states at the same time. Since this technique is based on the steady-state Schrödinger equation, the propagation of an electronic state is rather *ad hoc*. On the other hand, the non-adiabatic quantum MD method [90], which is formulated without the Born-Oppenheimer approximation, can currently handle a system with a few atoms. Certain new advances in the quantum MD method for heat transfer must be developed [91, 92].

Finally, the comparison with experiment is often crucial. Since most experiments in heat transfer deal with macroscopic quantities, it is not easy to evaluate simulation results. A few direct comparisons of the MD simulations to experiments have been reported in the heat transfer field such as the EXAFS study of LiBr effect on liquid-vapor interfacial phenomena [93, 94], or FT-ICR mass spectroscopic study on carbon clusters [95, 96].

7. NOMENCLATURE

A	constant in Tersoff/Brenner potential
a	potential parameter in Eq. (11)
a_1-a_4	potential parameters in Eq. (6)
B	constant parameter in Tersoff/Brenner potential
b_1-b_4	potential parameters in Eq. (6)
b_{ij}	function in Tersoff potential
c	constant in Tersoff/Brenner potential, speed of light
D	diffusivity, half width of cutoff function
D_e	potential depth in Tersoff/Brenner potential
$\tilde{D}_{\alpha\beta}$	rotation matrix
d	constant in Tersoff/Brenner potential
E_k	kinetic energy
$\boldsymbol{F}$	force vector
f	force
f_c	cutoff function
$g(\theta)$	a function in Tersoff/Brenner potential
h	constant in Tersoff/Brenner potential
$\hbar$	Planck's constant: 1.05459×10^{-34} Js
$I(\omega)$	transition rate

k spring constant of harmonic potential
k_B Boltzmann constant
L length of a calculation cell
m mass
N number density
n constant in Tersoff/Brenner potential, density of species
P pressure
$\tilde{p}_{\alpha\beta}$ instantaneous pressure tensor
q electric charge, heat flux
$\tilde{q}_\alpha$ $\alpha(x, y, z)$ component of energy flux
$\boldsymbol{R}$ position of molecule
R radius, intermolecular distance of oxygen, center of cutoff radius
R_0 nearest neighbor distance of solid crystal
R_e equilibrium intermolecular distance, equimolar dividing radius
R_S radius of surface of tension
r intermolecular distance
$\boldsymbol{r}$ position vector
S constant in Tersoff/Brenner potential
$S(R)$ modulation function for ST2 potential
T temperature
T_c critical temperature
T_{JUMP} temperature jump
T_t triplet temperature
t time
t_P time constant
U internal energy, fluid dynamics velocity
V volume
$V_A(r)$ an attractive potential function in Tersoff/Brenner potential
$V_R(r)$ a repulsive potential function in Tersoff/Brenner potential
$\boldsymbol{v}$ velocity vector
z coordinate perpendicular to the interface

Greek Symbols:
α absorption cross section, damping factor
β constant in Tersoff/Brenner potential
β_T isothermal compressibility
χ scaling factor
Δt time step of the finite difference integration
δ constant in Tersoff/Brenner potential, Tolman length
ε energy parameter of Lennard-Jones potential
ε_0 permittivity (dielectric constant) in vacuum = 8.8542×10^{-12} F/m = 8.8542×10^{-12} $C^2/(Nm^2)$
ε_i instantaneous energy of molecule i
Φ potential
ϕ pair potential

γ surface tension
λ constant in Tersoff/Brenner potential, thermal conductivity
μ shear viscosity
$\boldsymbol{\mu}$ dipole moment
θ angle, contact angle
ρ density
σ length parameter of Lennard-Jones potential
σ_F standard deviation of exiting force
τ time scale of non-dimensional Lennard-Jones system: $\tau = \sigma(m/\varepsilon)^{1/2}$
ω angular frequency
ω_D Debye frequency
ζ friction coefficient

Subscripts:
AR argon
C cutoff, control, center of fitting circle
G gas
H hydrogen
INT interaction of solid and liquid
i, j, k index of molecule
L liquid
LG liquid-gas
M position of negative point charge
N normal direction
OO oxygen-oxygen
S solid
SG solid-gas
SL solid-liquid
T tangential direction
V vapor
W solid wall

8. REFERENCES

1. J. O. Hirschfelder, C. F. Curtiss and R. B. Bird, *Molecular Theory of Gases and Liquids*, John Wiley & Sons, New York, 1954.
2. G. A. Bird, *Molecular Gas Dynamics and the Direct Simulation of Gas Flow*, Oxford University Press, New York, 1994.
3. C. Kittel, *Introduction to Solid State Physics*, 7th ed., John Wiley & Sons, New York, 1996.
4. G. Chen, Thermal Conductivity and Ballistic-Phonon Transport in the Cross-Plane Direction of Superlattices, *Phys. Rev. B*, vol. 57, no. 23, pp. 14958-14973, 1998.
5. M. P. Allen and D. J. Tildesley, *Computer Simulation of Liquids*, Oxford University Press, New York, 1987.

6. Nicolas, J. J., Gubbins, K. E., Streett, W. B. and Tildesley, D. J., Equation of State for the Lennard-Jones Fluid, *Molecular Physics*, vol. 37-5, pp. 1429-1454, 1979.
7. J. P. Hansen and L. Verlet, Phase Transitions of the Lennard-Jones System, *Phys. Rev.*, vol. 184, pp. 151-161, 1969.
8. M. J. P. Nijmeijer, A. F. Bakker, C. Bruin, and J. H. Sikkenk, A Molecular Dynamics Simulation of the Lennard-Jones Liquid-Vapor Interface, *J. Chem. Phys*., vol. 89, no. 6, pp. 3789-3792, 1988.
9. S. D. Stoddard and J. Ford, Numerical Experiments on the Stochastic Behavior of a Lennard-Jones Gas System, *Phys. Rev. A*, vol. 8, pp. 1504-1512, 1973.
10. F. H. Stillinger and A. Rahman, Improved Simulation of Liquid Water by Molecular Dynamics, *J. Chem. Phys.*, vol. 60, no. 4, pp. 1545-1557, 1974.
11. A. Ben-Naim and F. H. Stillinger, Aspects of the Statistical-Mechanical Theory of Water, in *Structure and Transport Processes in Water and Aqueous Solutions* (ed. R. A. Horne), Wiley-Interscience, New York, 1972.
12. H. J. C. Berendsen, J. P. M. Postma, W. F. van Gunsteren, J. Hermans, *in Intermolecular Forces* (ed. B. Pullmann), Reidel, Dordrecht, pp. 331-, 1981.
13. H. J. C. Berendsen, J. R. Grigera, and T. P. Straatsma, The Missing Term in Effective Pair Potentials, *J. Phys. Chem.*, vol. 91, no. 24, pp.6269-6271, 1987.
14. W. L. Jorgensen, J. Chandrasekhar, J. D. Madura, R. W. Impey and M. L. Klein, Comparison of Simple Potential Functions for Simulating Liquid Water, *J. Chem. Phys*., vol. 79, no. 2, pp. 926-935, 1983.
15. W. L. Jorgensen, Optimized Intermolecular Potential Functions for Liquid Alcohols, *J. Phys. Chem*., vol. 90, pp. 1276-1284, 1986.
16. O. Matsuoka, E. Clementi and M. Yoshimine, CI Study of the Water Dimer Potential Surface, *J. Chem. Phys.*, vol. 64, no. 4, pp. 1351-1361, 1976.
17. V. Carravetta and E. Clementi, Water-Water Interaction Potential: An Approximation of the Electron Correlation Contribution by a Function of the SCF Density Matrix, *J. Chem. Phys*., vol. 81, no. 6, pp. 2646-2651, 1984.
18. J. Alejandre, D. J. Tildesley, and G. A. Chapela, Molecular Dynamics Simulation of the Orthobaric Densities and Surface Tension of Water, *J. Chem. Phys*., vol. 102, no. 11, pp. 4574-4583, 1995.
19. L. X. Dang, and T-M. Chang, Molecular Dynamics Study of Water Clusters, Liquid, and Liquid-Vapor Interface of Water with Many-Body Potentials, *J. Chem. Phys*., vol. 106, no. 19, pp. 8149-8159, 1997.
20. U. Niesar, G. Corongiu, E. Clementi, G. R. Kneller and D. K. Bhattacharya, Molecular Dynamics Simulations of Liquid Water Using the NCC ab initio Potential, *J. Phys. Chem*., vol. 94, no. 20, pp. 7949-7956, 1990.
21. D. N. Bernardo, Y. Ding, K. K-Jespersen and R. M. Levy, An Anisotropic Polarizable Water Model: Incorporation of All-Atom Polarizabilities into Molecular Mechanics Force Fields, *J. Phys. Chem.*, vol. 98, pp. 4180-4187, 1994.
22. L. X. Dang and B. M. Pettitt, Simple Intramolecular Model Potentials for Water, *J. Phys. Chem.*, vol. 91, no. 12, pp. 3349-3354, 1987.
23. J. Anderson, J. J. Ullo and S. Yip, Molecular Dynamics Simulation of

Dielectric Properties of Water, *J. Chem. Phys.*, vol. 83, no. 3, pp. 1726-1732, 1987.
24. F. H. Stillinger and T. A. Weber, Computer Simulation of Local Order in Condensed Phase of Silicon, *Phys. Rev. B*, vol. 31, no. 8, pp. 5262-5271, 1985.
25. J. Tersoff, New Empirical Approach for the Structure and Energy of Covalent Systems, *Phys. Rev. B*, vol. 37, no. 12, pp. 6991-7000, 1988.
26. J. Tersoff, Empirical Interatomic Potential for Silicon with Improved Elastic Properties, *Phys. Rev. B*, vol. 38, no. 14, pp. 9902-9905, 1988.
27. J. Tersoff, Modeling Solid-State Chemistry: Interatomic Potentials for Multicomponent Systems, *Phys. Rev. B*, vol. 39, no. 8, pp. 5566-5568, 1989.
28. D. W. Brenner, Empirical Potential for Hydrocarbons for Use in Simulating the Chemical Vapor Deposition of Diamond Films, *Phys. Rev. B*, vol. 42, pp.9458-9471, 1990.
29. Y. Yamaguchi and S. Maruyama, A Molecular Dynamics Simulation of the Fullerene Formation Process, *Chem. Phys. Lett.*, vol. 286-3,4, pp. 336-342, 1998.
30. S. Maruyama and Y. Yamaguchi, A Molecular Dynamics Demonstration of Annealing to a Perfect C_{60} Structure, *Chem. Phys. Lett.*, vol. 286-3,4, pp. 343-349, 1998.
31. D. H. Tsai, The Virial Theorem and Stress Calculation in Molecular Dynamics, *J. Chem. Phys.*, vol. 70, no. 3, pp. 1375-1382, 1979.
32. T. Ikeshoji, B. Hafskjold and H. Furuholt, Molecular-Level Calculation Scheme for Pressure and Energy Flux in Heterogeneous Systems of Planar and Spherical Symmetry, *Molecular Physics*, 1999, submitted.
33. J. C. Tully, Dynamics of Gas-Surface Interactions: 3D Generalized Langevin Model Applied to fcc and bcc Surfaces, *J. Chem. Phys.*, vol. 73, no. 4, pp. 1975-1985, 1980.
34. J. Blömer and A. E. Beylich, MD-Simulation of Inelastic Molecular Collisions with Condensed Matter Surfaces, *Proceedings of 20th International Symposium on Rarefied Gas Dynamics*, Beijing, China, August 19-23, 1996, pp. 392-397, Peking University Press, Beijing, 1997.
35. S. Maruyama, and T. Kimura, A Molecular Dynamics Simulation of a Bubble Nucleation on Solid Surface, *Proceedings of 5th ASME-JSME Thermal Engineering Joint Conference*, San Diego, U.S.A., March 15-19, 1999, AJTE99-6511, 1999.
36. S. Maruyama and T. Kimura, A Study on Thermal Resistance over a Solid-Liquid Interface by the Molecular Dynamics Method, *Thermal Sci. Eng.*, vol. 7, no. 1, pp. 63-68, 1999.
37. T. Tokumasu and Y. Matsumoto, Parallel Computing of Diatomic Molecular Rarefied Gas Flows, *Parallel Computing*, vol. 23, pp. 1249-1260, 1997.
38. T. Tokumasu and Y. Matsumoto, Dynamic Molecular Collision (DMC) Model of Diatomic Molecules for DSMC Calculation, *Proceedings of 21st International Symposium on Rarefied Gas Dynamics*, vol. 2, in print, 1998.
39. N. Yamanishi and Y. Matsumoto, A New Model for Diatomic Molecules Scattering from Solid Surfaces, *Proceedings of 20th International Symposium on Rarefied Gas Dynamics*, Beijing, China, August 19-23, 1996,

pp. 381-386, Peking University Press, Beijing, 1997.
40. H. C. Anderson, Molecular Dynamics Simulations at Constant Pressure and/or Temperature, *J. Chem. Phys.*, vol. 72, no. 4, pp. 2384-2393, 1980.
41. S. Nosé, A Unified Formulation of the Constant Temperature Molecular Dynamics Methods, *J. Chem. Phys.*, vol. 81, no. 1, pp. 511-519, 1984.
42. W. G. Hoover, Canonical Dynamics: Equilibrium Phase-Space Distributions, *Phys. Rev. A*, vol. 31, no. 3, pp. 1695-1697, 1985.
43. M. Parrinello and A. Rahman, Crystal Structure and Pair Potentials: a Molecular Dynamics Study, *Phys. Rev. Lett.*, vol. 45, pp. 1196-1199, 1980.
44. M. Parrinello and A. Rahman, Polymorphic Transitions in Single Crystal: a New Molecular Dynamics Method, *J. Appl. Phys.*, vol. 52, pp. 7182-7190, 1981.
45. H. J. C. Berendsen, J. P. M. Postma, W. F. van Gunsteren, A. DiNola, and J. R. Haak, Molecular dynamics with coupling to an external bath, *J. Chem. Phys.*, vol. 81, no. 8, pp. 3684-3690, 1984.
46. P. H. Berens and K. R. Wilson, Molecular Dynamics and Spectra. I. Diatomic Rotation and Vibration, *J. Chem. Phys.*, vol. 74, no. 9, pp. 4872-4884, 1981.
47. S. Matsumoto and S. Maruyama, Far-Infrared Spectrum of Water by Molecular Dynamics Method, *Proceedings of the Second JSME-KSME Thermal Engineering Conference*, Kitakyushu, Japan, October 19-21, 1992, Vol. 3, pp. 61-64, 1992.
48. S. Maruyama, S. Matsumoto, and A. Ogita, Surface Phenomena of Molecular Clusters by Molecular Dynamics Method, *Thermal Sci. Eng.*, vol. 2, no. 1, pp. 77-84, 1994.
49. S. Maruyama, S. Matsumoto, M. Shoji and A. Ogita, A Molecular Dynamics Study of Interface Phenomena of a Liquid Droplet, *Heat Transfer 1994: Proceedings of the Tenth International Heat Transfer Conference*, Brighton, U.K., August 14-18, 1994, Vol. 3, pp. 409-414, Taylor & Francis, Washington D.C., 1994.
50. S. M. Thompson, K. E. Gubbins, J. P. R. B. Walton, R. A. R. Chantry, and J. S. Rowlinson, A Molecular Dynamics Study of Liquid Drops, *J. Chem. Phys.*, vol. 81, no. 1, pp. 530-542,1984.
51. M. J. P. Nijmeijer, C. Bruin, A. B. van Woerkom, and A. F. Bakker, Molecular Dynamics of the Surface Tension of a Drop, *J. Chem. Phys.*, vol. 96, no. 1, pp. 565-576, 1992.
52. M. J. Haye and C. Bruin, Molecular Dynamics Study of the Curvature Correction to the Surface Tension, *J. Chem. Phys.*, vol. 100, no. 1, pp. 556-559, 1994.
53. R. M. Townsend and S. A. Rice, Molecular Dynamics Studies of the Liquid-Vapor Interface of Water, *J. Chem. Phys.*, vol. 94, no. 3, pp. 2207-2218, 1991.
54. I. Tanasawa, Recent Advances in Condensation Heat Transfer, *Heat Transfer 1994: Proceedings of the Tenth International Heat Transfer Conference*, Brighton, U.K., August 14-18, 1994, Vol. 1, pp. 297-312, Taylor & Francis, Washington D.C., 1994.
55. K. Yasuoka, M. Matsumoto and Y. Kataoka, Evaporation and Condensation

at a Liquid Surface. I. Argon, *J. Chem. Phys.*, vol. 101, no. 9, pp. 7904-7911, 1994.
56. M. Matsumoto, K. Yasuoka and Y. Kataoka, Evaporation and Condensation at a Liquid Surface. II. Methanol, *J. Chem. Phys.*, vol. 101, no. 9, pp. 7911-7917, 1994.
57. M. Matsumoto, K. Yasuoka and Y. Kataoka, Molecular Mechanism of Evaporation and Condensation, *Thermal Sci. Eng*., vol. 3, no.3, pp. 27-31, 1995.
58. M. Matsumoto and S. Fujikawa, Nonequilibrium Vapor Condensation: Molecular Simulation and Shock-Tube Experiment, *Micro. Thermophys. Eng.*, vol. 1, no. 2, pp. 119-126, 1997.
59. S. Fujikawa, M. Kotani and N. Takasugi, Theory of Film Condensation on Shock-Tube Endwall behind Reflected Shock Wave (Theoretical Basis for Determination of Condensation Coefficient), *JSME Int. J*., Ser. B, vol. 40, no. 1, pp. 159-165, 1997.
60. T. Tsuruta, H. Tanaka, K. Tamashima and T. Masuoka, Condensation Coefficient and Interphase Mass Transfer, *International Symposium on Molecular and Microscale Heat Transfer in Materials Processing and Other Applications* (ed. I. Tanasawa and S. Nishio), Begell House, New York, pp. International Center Heat Mass Transfer Symposium, Yokohama, pp. 229-240, 1997.
61. M. Kotani, T. Tsuzuyama, Y. Fujii and S. Fujikawa, Nonequilibrium Vapor Condensation in Shock Tube, *JSME Int. J*., Ser. B, vol. 41, no. 2, pp. 436-440, 1998.
62. M. Matsumoto, Molecular Dynamics of Fluid Phase Change, *Fluid Phase Equilibria*, vol. 144, pp. 307-314, 1998.
63. V. P. Carey and S. M. Oyumi, Condensation Growth of Single and Multiple Water Microdroplets in Supersaturated Steam: Molecular Simulation Predictions, *Micro. Thermophys. Eng.*, vol. 1, no.1, pp. 31-38, 1997.
64. V. E. B. Dussan, On the Spreading of Liquids on Solid Surfaces: Static and Dynamic Contact Lines, *Ann. Rev. Fluid Mech.*, vol. 11, pp. 371-400, 1979.
65. J. Koplik and J. R. Banavar, Continuum Deductions from Molecular Hydrodynamics, *Ann. Rev. Fluid Mech*., vol. 27, pp. 257-292, 1995.
66. S. Matsumoto, S. Maruyama, and H. Saruwatari, A Molecular Dynamics Simulation of a Liquid Droplet on a Solid Surface, *Proceedings of the ASME-JSME Thermal Engineering Joint Conference*, Maui, U.S.A., March 19-24, 1995, Vol. 2, pp. 557-562, 1995.
67. S. Maruyama, T. Kurashige, S. Matsumoto, Y. Yamaguchi and T. Kimura, Liquid Droplet in Contact with a Solid Surface, *Micro. Thermophys. Eng*., vol. 2, no.1, pp. 49-62, 1998.
68. J. N. Israelachvili, *Intermolecular and Surface Forces*, Academic Press, London, 1985.
69. S. Maruyama and T. Kimura, A Molecular Dynamics Simulation of a Bubble Nucleation on Solid Surface, *Proceeding of the Eurotherm Seminar n°57 on Microscale Heat Transfer*, Poitiers, France, July 8-10, 1998, in print, 1999.
70. G. Saville, Computer Simulation of the Liquid-Solid-Vapour Contact Angle,

J. Chem. Soc. Faraday Trans. 2, vol. 73, pp. 1122-1132, 1977.
71. M. J. P. Nijmeijer, C. Bruin and A. F. Bakker, Wetting and Drying of an Inert Wall by a Fluid in a Molecular-Dynamics Simulation, *Physical Rev. A*, vol. 42, no. 10, pp. 6052-6059, 1990.
72. J. H. Sikkenk, J. O. Indekeu, J. M. J. van Leeuwen, E. O. Vossnack and A. F. Bakker, Simulation of Wetting and Drying at Solid-Fluid Interfaces on the Delft Molecular Dynamics Processor, *J. Statistical Physics*, vol. 52, nos. 1/2, pp. 23-44, 1988.
73. P. A. Thompson, W. B. Brickerhoff and M. O. Robbins, Microscopic Studies of Static and Dynamic Contact Angle, *J. Adhesion Sci Technol.*, vol. 7, no. 6, pp. 535-554, 1993.
74. Fan, C. F. and Cagin, T., 1995, Wetting of Crystalline Polymer Surfaces: A Molecular Dynamics Simulation, *J. Chem. Phys*., vol. 103, no 20, pp. 9053-9061.
75. S. Kotake and S. Wakuri, Molecular Dynamics Study of Heat Conduction in Solid Materials, *JSME Int. J.*, Series B, vol. 37, no.1, pp. 103-108, 1994.
76. B. Hafskjold and T. Ikeshoji, On the Molecular Dynamics Mechanism of Thermal Diffusion in Liquids, *Molecular Physics*, vol. 80, no. 6, pp. 1389-1412, 1993.
77. T. Ikeshoji and B. Hafskjold, Non-Equilibrium Molecular Dynamics Calculations of Heat Conduction in Liquid and through Liquid-Gas Interface, *Molecular Physics*, vol. 81, no. 2, pp. 251-261, 1994.
78. K. Yasuoka and M. Matsumoto, Molecular Dynamics of Homogeneous Nucleation in the Vapor Phase. I. Lennard-Jones Fluid, *J. Chem. Phys*., vol. 109, no. 19, pp. 8451-8462, 1998.
79. K. Yasuoka and M. Matsumoto, Molecular Dynamics of Homogeneous Nucleation in the Vapor Phase. II. Water, *J. Chem. Phys*., vol. 109, no. 19, pp. 8463-8470, 1998.
80. K. Yasuoka and M. Matsumoto, Molecular Dynamics Simulation of Homogeneous Nucleation in Supersaturated Water Vapor, *Fluid Phase Equilibria*, vol. 144, no. 1-2, pp. 369-376, 1998.
81. Y. Viisanen, R. Stray and H. Reiss, Homogeneous Nucleation Rates for Water, *J. Chem. Phys.*, vol. 99, no. 6, pp. 4680-4692, 1993.
82. T. Ikeshoji, B. Hafskjold, Y. Hashi and Y. Kawazoe, Molecular Dynamics Simulation for the Cluster Formation Process of Lennard-Jones Particles: Magic Numbers and Characteristic Features, *J. Chem. Phys*., vol. 105, no. 12, pp. 5126-5137, 1996.
83. T. Ikeshoji, B. Hafskjold, Y. Hashi and Y. Kawazoe, Molecular Dynamics Simulation for the Formation of Magic-Number Clusters with the Lennard-Jones Potential, *Phys. Rev. Lett.*, vol. 76, no. 11, pp. 1792-1795, 1996.
84. T. Kinjo and M. Matsumoto, Cavitation Processes and Negative Pressure, *Fluid Phase Equilibria*, 144, pp. 343-350, 1998.
85. J. Tamba, T. Ohara and T. Aihara, MD Study on Interfacelike Phenomena in Supercritical Fluid, *Micro. Thermophys. Eng.*, vol. 1, no.1, pp. 19-30, 1997.
86. T. Ohara and T. Aihara, MD Study on Dynamic Structure of Water, *International Symposium on Molecular and Microscale Heat Transfer in*

Materials Processing and Other Applications (ed. I. Tanasawa and S. Nishio), Begell House, New York, pp. 75-84, 1997.
87. Y. Yamaguchi, S. Maruyama and S. Hori, A Molecular Dynamics Simulation of Metal-Containing Fullerene Formation, *Proceedings of 5th ASME-JSME Thermal Engineering Joint Conference*, San Diego, U.S.A., March 15-19, 1999, AJTE99-6508, 1999.
88. S. Hirai, K. Okazaki, S. Kuraoka and K. Kawamura, Molecular Dynamics Simulation for the Formation of Argon Clathrate-Hydrate Structure, *Micro. Thermophys. Eng.*, vol. 1, no. 4, pp. 293-301, 1997.
89. R. Car and M. Parrinello, Unified Approach for Molecular Dynamics and Density-Functional Theory, *Phys. Rev. Lett*, vol. 55, no. 22, pp. 2471-2474, 1985.
90. U. Saalmann and R. Schmidt, Non-Adiabatic Quantum Molecular Dynamics: Basic Formalism and Case Study, *Z. Phys. D*, vol. 38, pp. 153-163, 1996.
91. M. Shibahara and S. Kotake, Quantum Molecular Dynamics Study on Light-to-Heat Absorption Mechanism: Two Metallic Atom System, *Int. J. Heat Mass Transfer*, vol. 40, no. 13, pp. 3209-3222, 1997.
92. M. Shibahara and S. Kotake, Quantum molecular dynamics study of light-to-heat absorption mechanism in atomic systems, *Int. J. Heat Mass Transfer*, vol. 41, no. 6-7, pp. 839-849, 1998.
93. H. Daiguji and E. Hihara, An EXAFS (Extended X-ray Absorption Fine Structure) Study of Lithium Bromide Aqueous Solutions Using Molecular Dynamics Simulation, *Heat Transfer Japanese Research*, in print, 1999.
94. H. Daiguji and E. Hihara, Molecular Dynamics Study of the Water Vapor Absorption into Aqueous Electrolyte Solution, *Micro. Thermophys. Eng.*, vol. 3, no. 2, pp. 151-165, 1999.
95. S. Maruyama, T. Yoshida, M. Kohno and M. Inoue, FT-ICR Studies of Laser Desorbed Carbon Clusters, *Proceedings of 5th ASME-JSME Thermal Engineering Joint Conference*, San Diego, U.S.A., March 15-19, 1999, JTE99-6513, 1999.
96. S. Maruyama, Y. Yamaguchi, M. Kohno and T. Yoshida, Formation Process of Empty and Metal-Containing Fullerene. —Molecular Dynamics and FT-ICR Studies, *Fullerene Science and Technology*, vol. 7, no. 4, pp. 621-636, 1999.